Petroleum Science 23 (2026) 7578–7601

Contents lists available at ScienceDirect

Petroleum Science

journal homepage: www.keaipublishing.com/en/journals/petroleum-science

Original Paper

Three-dimensional fracture characteristics and propagation behavior of shale in supercritical carbon dioxide fracturing experiments under different geo-stress conditions

Wang-Xing Hong [a], Sheng-Qi Yang [b,c,*], Bo-Wen Sun [b], Xiao-Hua Xu [a], Chao Zhu [d,e], Wen-Ling Tian [c], P.G. Ranjith [f]

[a] State Key Laboratory of Intelligent Construction and Healthy Operation and Maintenance of Deep Underground Engineering, China University of Mining and Technology, Xuzhou, 221116, Jiangsu, China
[b] Zhejiang Key Laboratory of Rock Mechanics and Geohazards, School of Civil Engineering, Shaoxing University, Shaoxing, 312000, Zhejiang, China
[c] School of Mechanics and Civil Engineering, China University of Mining and Technology, Xuzhou, 221116, Jiangsu, China
[d] State Key Laboratory of Coal Mine Disaster Dynamics and Control, Chongqing University, Chongqing, 400044, China
[e] School of Resources and Safety Engineering, Chongqing University, Chongqing, 400044, China
[f] Deep Earth Energy Research Laboratory, Department of Civil Engineering, Monash University, Melbourne, VIC, 3800, Australia

ARTICLE INFO

Article history:
Received 1 December 2025
Received in revised form
26 January 2026
Accepted 3 July 2026
Available online 9 July 2026

Edited by Min Li

Keywords:
Shale
Supercritical carbon dioxide fracturing
Three-dimensional fracture characteristics
Fracture propagation behavior
Geo-stress condition

ABSTRACT

During shale gas production, the enhancement of stimulated reservoir volume is contingent upon the establishment of a three-dimensional (3D) complex fracture network. Supercritical carbon dioxide (SC-CO_2) holds great promise as an emerging fracturing fluid, owing to its unique advantages in reducing breakdown pressure, forming high-roughness fractures, and inducing multiple fractures. However, the influence of geo-stress conditions on the 3D fracture characteristics and propagation behavior of shale using SC-CO_2 fracturing remains poorly understood and merits further investigation. In this study, laboratory-scale true triaxial fracturing tests were conducted on Longmaxi Formation shale, with variables including fluid type, horizontal stress difference, and stress regime. Deep learning methods offer significant advantages in accurately identifying minute fractures induced by SC-CO_2 fracturing, and thus the U-Net deep learning model and computed tomography (CT) technology were combined in this study to conduct 3D reconstruction and digital quantitative analysis of fractures. Additionally, acoustic emission (AE) signals of fractures during the shale fracturing process were collected and analyzed. The results indicated that: (1) The ability of SC-CO_2 to activate bedding planes and the phase transition effect of CO_2 were the two core mechanisms responsible for the generation of such rough and complex fractures during SC-CO_2 fracturing. (2) A large horizontal stress difference coefficient would reduce the roughness and complexity of fractures induced by SC-CO_2 fracturing. As the horizontal stress difference increased, the fracture propagation behavior of shale in SC-CO_2 fracturing experiments gradually shifted from being dominated by bedding planes to being dominated by geo-stress. (3) The stress regimes (normal faulting or strike-slip faulting) exerted minimal influence on the complexity of the fracture network induced by SC-CO_2 fracturing because of the small magnitude difference between the maximum and intermediate principal stresses. The fracture propagation behavior of shale under the above two stress regimes remained significantly governed by the bedding plane. (4) The fracture propagation patterns when a fracture induced by SC-CO_2 fracturing approached a shale bedding plane were summarized as follows: activating, deflecting, penetrating, or composite. These findings provided a reference for the optimized design of SC-CO_2 fracturing schemes for shale reservoirs under different geo-stress conditions.
© 2026 The Authors. Publishing services by Elsevier B.V. on behalf of KeAi Communications Co. Ltd. This is an open access article under the CC BY-NC-ND license (http://creativecommons.org/licenses/by-nc-nd/4.0/).

* Corresponding author.
E-mail address: 2024000008@usx.edu.cn (S.-Q. Yang).
Peer review under the responsibility of China University of Petroleum (Beijing).

https://doi.org/10.1016/j.petsci.2026.07.004
1995-8226/© 2026 The Authors. Publishing services by Elsevier B.V. on behalf of KeAi Communications Co. Ltd. This is an open access article under the CC BY-NC-ND license (http://creativecommons.org/licenses/by-nc-nd/4.0/).

1. Introduction

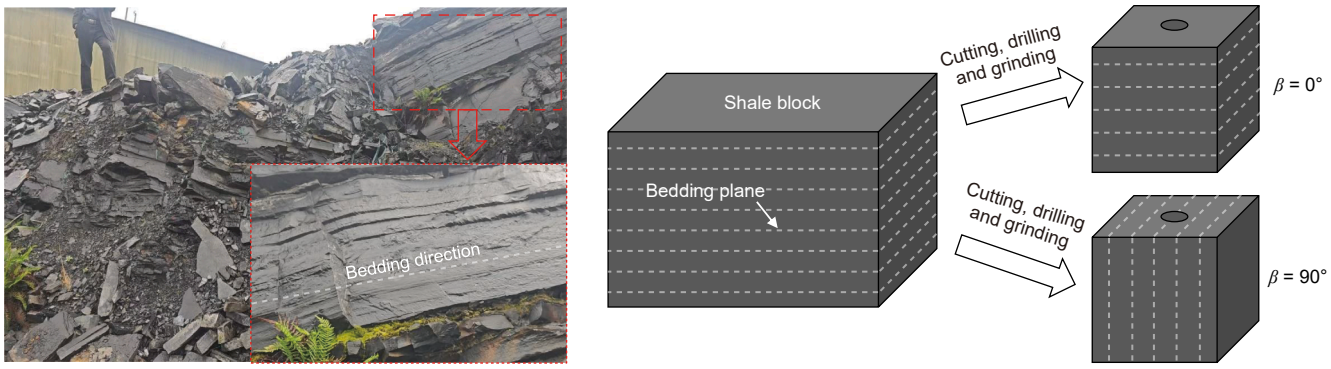
Against the backdrop of the growing global energy demand, prioritizing the vigorous development of clean, efficient, and abundant shale gas resources is a reliable approach (Stueck et al., 2016). Hydraulic fracturing technology for reservoir stimulation is widely recognized as one of the key steps in current shale gas extraction projects (Josifovic et al., 2016). Among various fracturing fluids, slick-water, the most common water-based fracturing fluid used in commercial shale gas development (Estrada et al., 2016), requires a large amount of water during its preparation. However, according to a report by the World Resources Institute, the global distribution of shale gas resources is uneven, and most shale gas resources are not located in water-abundant areas (Reig et al., 2014). The massive water consumption will obviously restrict shale gas production in water-scarce areas (Nicot and Scanlon, 2012; Scanlon et al., 2014; Shi et al., 2020). Moreover, the flowback rate of water-based fracturing fluids is usually low. This not only may cause reservoir damage and thus reduce shale gas recovery but also may lead to environmental issues related to water pollution (Estrada et al., 2016; Yang et al., 2024; Zhang et al., 2024). Therefore, the development of waterless fracturing technologies has become an urgent need in the field of shale gas development.

Meanwhile, the continuous increase in atmospheric CO_2 concentration has intensified the issue of global warming and caused a series of environmental disasters, such as rising sea levels, an increase in extreme weather events, and ecological imbalances (IPCC et al., 2022). Coincidentally, carbon dioxide, a major component of greenhouse gases, exhibits unique physicochemical properties when it reaches a supercritical state, including liquid-like density, gas-like viscosity, no capillary force, and good compatibility with hydrocarbons, which is expected to contribute to shale gas production (Lyu et al., 2021; Zang et al., 2024). SC-CO_2 fracturing has the following advantages over traditional hydraulic fracturing: (1) SC-CO_2 fracturing generates a rougher and more complex fracture network, leading to higher permeability. (2) No water is involved in SC-CO_2 fracturing, which not only conserves water resources but also reduces reservoir damage caused by water. (3) The adsorption capacity of SC-CO_2 in shale is higher than that of methane. This can improve single-well production and recovery by displacing methane molecules adsorbed in shale. (4) After SC-CO_2 fracturing, part of the CO_2 is retained in the formation through mechanisms such as diffusion, displacement, and adsorption, thereby achieving geological sequestration of carbon dioxide (Middleton et al., 2014, 2015; Rubin et al., 2015; Rani et al., 2019; Zhou et al., 2019; Mojid et al., 2021; Zhao et al., 2023; Yang et al., 2025a). In summary, in the face of the dual challenges of energy shortage and global warming, the application of SC-CO_2 in shale gas extraction has enormous potential value (Ishida et al., 2012; Pei et al., 2015; Hu et al., 2019; Kumar et al., 2024). It not only reduces the high dependence on water resources during shale gas reservoir fracturing but also helps accelerate the global carbon neutrality process.

In shale gas development projects, fractures formed by fracturing are the main flow channels for natural gas. Shale gas production is directly determined by the fracture characteristics and propagation behavior, which have become a research hotspot nowadays. At the laboratory scale, the most commonly used analytical methods for fractures currently include profile gauges, 3D laser scanning, AE monitoring, CT scanning, and high-speed cameras. Many scholars observed that the fracture surfaces generated by SC-CO_2 fracturing were more complex and rugged than those generated by hydraulic fracturing by using the digital radiography (Zhang et al., 2017; Yang et al., 2025b), profile gauge (Jia et al., 2018), and 3D laser scanning (Zhao et al., 2018). Based on slices of the CT scanning, scholars found that SC-CO_2 fracturing fractures were irregular multi-fractures, with the potential to connect with natural fractures and bedding planes, forming a complex fracture network (Zhou et al., 2016; Zhang et al., 2017). And the initiation position and propagation directions of SC-CO_2 fracturing fractures were primarily along the weak structural planes in shale or the directions of pre-existing fractures (Jiang et al., 2018). However, limited fracture complexity was observed in specimens without pre-existing cracks (Al Shafloot et al., 2021). Furthermore, the fracture propagation behavior exhibited phased characteristics, as demonstrated by AE monitoring during SC-CO_2 fracturing (Zhou et al., 2018a). The fracturing process in transparent specimens was recorded by means of a high-speed camera, and the fracture propagation speed of SC-CO_2 fracturing was found to be two orders of magnitude greater than that of hydraulic fracturing (Zhou et al., 2018b).

For the quantitative analysis of fractures in CT images, it is necessary to separate fracture voxels from non-fracture constituents such as minerals and pores, a procedure referred to as segmentation. The traditional threshold segmentation method is widely used for CT image segmentation (Iassonov et al., 2009; Ramandi et al., 2016; Van Eijnatten et al., 2018), but this method usually requires manual operation, which is time-consuming and may lead to significant errors (Lei and Fan, 2024). In recent years, deep learning methods have become powerful processing tools for detecting and segmenting cracks in CT images. A fully convolutional neural network (U-Net) deep learning segmentation algorithm was introduced for high-resolution CT images to accurately distinguish the pore space and fractures (Pham et al., 2023; He et al., 2024), and even various minerals in rocks (Tang et al., 2022). However, obtaining high-resolution CT images typically means high scanning costs, complex scanning procedures, and smaller sample sizes. In laboratory scale model experiments in the field of petroleum engineering, the size of rock samples was usually large, which usually resulted in reduced CT scanning resolution. Furthermore, the fractures induced by SC-CO_2 fracturing were extremely narrow, with a fracture width typically less than 50 μm (Li and Zhang, 2019), making it difficult to extract fractures completely using conventional segmentation methods. Therefore, how to identify minute fractures in these low-resolution CT scans remains a challenging task.

Shale is characterized by the presence of discontinuities, including bedding planes, lithologic interfaces and natural fractures. The connectivity between these discontinuities and fracturing fractures affects the complexity of the resulting fracture network, thereby significantly influencing the stimulated reservoir volume of shale formations (Ranjith et al., 2019; Tan et al., 2024; Zhong et al., 2024; Gong et al., 2025). Consequently, extensive research has been conducted to elucidate the interaction mechanisms between fracturing fractures and discontinuities, yielding important insights (Dan et al., 2015; Llanos et al., 2017; Hou et al., 2018; Zhang et al., 2022; Cong et al., 2024). When a fracturing fracture encounters an interface, four possible propagation patterns may occur near the bedding plane: arresting pattern, deflecting pattern, penetrating pattern and composite pattern (Zhang et al., 2023). Furthermore, the interaction mechanism between fracturing fractures and discontinuities is influenced by factors such as in-situ stress, the cement strength of bedding planes, fracturing fluid type and approach angle between hydraulic fractures and discontinuities (Tan et al., 2018). For the in-situ stress differences, at low stress differences, hydraulic fractures tended to deflect toward natural fractures and bedding planes; conversely, larger stress differences facilitated hydraulic fractures to cross discontinuities (Hou and Cui, 2023; Li et al.,



(a) Sampling site of shale blocks **(b)** Schematic of shale specimens for fracturing test with two bedding inclinations

Fig. 1. Sampling locations and processing schematic of shale blocks.

2014; Bennour et al., 2015). For the cement strength of bedding planes, hydraulic fractures can penetrate strongly cemented interfaces but open sufficient weak cemented interfaces to allow fracturing fluid to migrate within them (Tan et al., 2017). For the fracturing fluid type, in the case of coal-rock masses, hydraulic fracturing produced a single and straight fracture that directly penetrates the coal-rock interface. In contrast, SC-CO_2 fracturing formed complex fractures with numerous secondary fractures, but failed to penetrate the coal-rock interface (Jiang et al., 2023). However, in the case of the tight sandstone specimens containing multiple bedding planes and natural fractures, SC-CO_2 likely promoted the dilation or shearing of bedding planes and natural fractures, resulting in a complex fracture network even under a high horizontal differential stress (Zou et al., 2018). For the approach angle between hydraulic fractures and discontinuities, the inclination of natural fractures was conducive to the formation of shear fractures and thus to the deflection of the expansion direction of hydraulic fractures (Qiu et al., 2024). In addition, the main fracture propagating almost parallel to the bedding plane corresponded to a lower breakdown pressure, whereas the main fracture propagating almost perpendicularly to the bedding plane corresponded to a higher breakdown pressure (Zhang et al., 2019; Guo et al., 2021).

In summary, previous studies have concentrated on the local characteristics of fracture surfaces induced by SC-CO_2 fracturing. However, the fracture propagation behavior of shale using SC-CO_2 fracturing under different geo-stress conditions from a 3D perspective has not been thoroughly studied. Therefore, this study conducted laboratory-scale true triaxial fracturing tests on Longmaxi Formation shale. After that, the deep learning method combined with CT technology was used for the 3D reconstruction and digital quantitative analysis of fractures. Combined with AE analysis techniques, three critical variables, namely fluid type, horizontal stress difference, and stress regime, were selected as the core focus of this study to clarify their respective impacts on the fracturing-induced fracture characteristics and propagation behavior of shale specimens. This study could provide references for the optimized design of SC-CO_2 fracturing schemes for shale reservoirs under different geo-stress conditions in engineering practice.

2. Experimental materials and methods

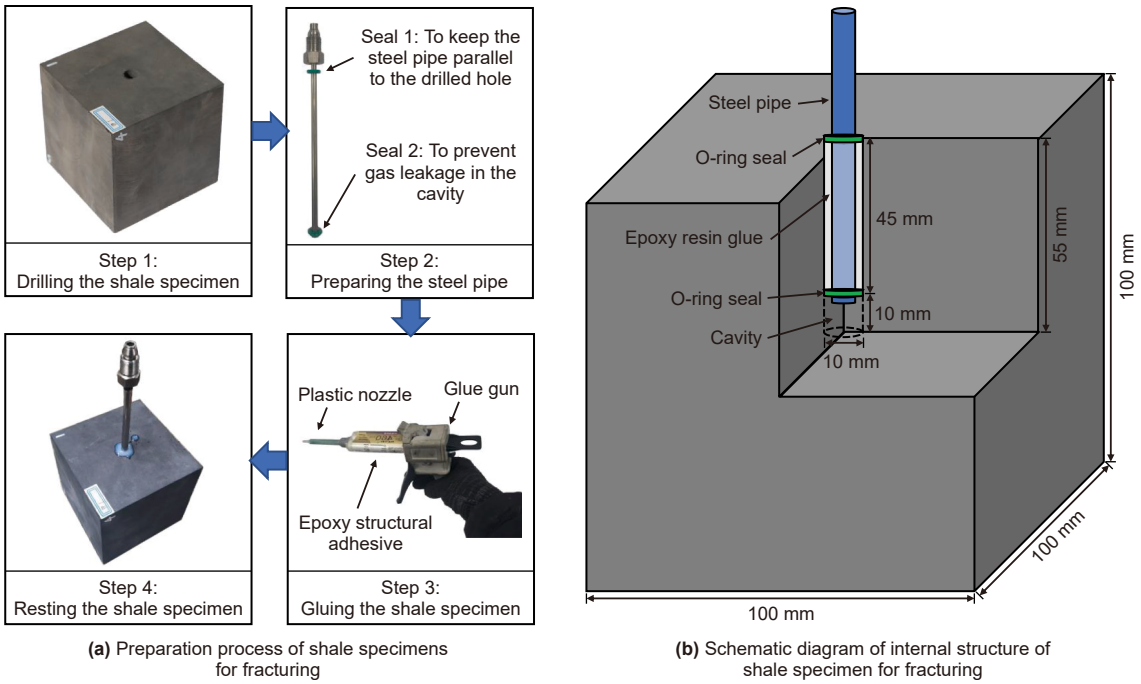
2.1. Shale specimens

The shale specimens tested in this study were collected from an open-pit mine near Well Ning-201 in the Changning Shale Gas Field. The shale specimens belong to the Lower Silurian Longmaxi Formation, the key stratum for shale gas exploration in China. Previous studies showed that existing faults, fractures, and weak layer interfaces may significantly impact the propagation of hydraulic fractures in practical scenarios (Wang et al., 2017; Yang et al., 2020; Xie et al., 2023). Therefore, to minimize the interference of natural cracks in the test results, relatively intact outcrop shale blocks were chosen. As illustrated in Fig. 1, these blocks exhibited no obvious fractures, featured well-cemented bedding planes, and were structurally intact. Subsequently, the shale blocks underwent cutting, drilling, and surface grinding processes. Finally, shale specimens with different bedding inclinations ($\beta = 0°$ or 90°) were obtained for laboratory fracturing experiments. The shale specimen exhibiting parallel bedding planes was designated as $\beta = 0°$; and the shale specimen displaying vertical bedding planes was designated as $\beta = 90°$.

As shown in Fig. 2, the preparation process of shale specimens for laboratory fracturing experiments involves approximately four steps: (I) Process the shale block into a cube measuring $100 \times 100 \times 100$ mm, grind the end faces of the specimen to be flat, and drill a simulated wellbore with a diameter of 10 mm and a depth of 55 mm on the top surface of the block. (II) Use a steel tube to simulate the perforation tunnels. The steel tube has an outer diameter of 6 mm and an inner diameter of 4 mm. Two O-rings are installed on the steel tube: the upper O-ring is used to fix the position of the steel tube in the fracturing hole, while the lower O-ring is used to prevent the epoxy structural adhesive from flowing into the cavity. (III) Seal the gap between the steel tube and the fracturing hole with epoxy structural adhesive. (IV) Let the shale specimen sealed with adhesive stand for 3 days before conducting the fracturing experiment.

2.2. Experimental equipment

The laboratory fracturing experiments conducted in this study were performed on a true triaxial SC-CO_2 fracturing test system. As shown in Fig. 3, the test system consisted of three primary modules, including the SC-CO_2 generation and injection system, the true triaxial stress loading system, and the AE monitoring system. Specifically, (1) The SC-CO_2 generation and injection system was mainly composed of a CO_2 gas cylinder, a gas booster pump, a gas heating device, a high-pressure storage tank, a plunger pump, and injection pipelines. Among them, the CO_2 gas cylinder contained industrial-grade carbon dioxide gas with a purity of more than 99.5%, and multiple CO_2 gas cylinders were prepared to ensure sufficient gas supply. The gas booster pump was capable of pressurizing the CO_2 gas to the predetermined initial pressure,



(a) Preparation process of shale specimens for fracturing

(b) Schematic diagram of internal structure of shale specimen for fracturing

Fig. 2. Schematic diagram of the preparation process and internal structure of shale specimens for laboratory fracturing experiments.

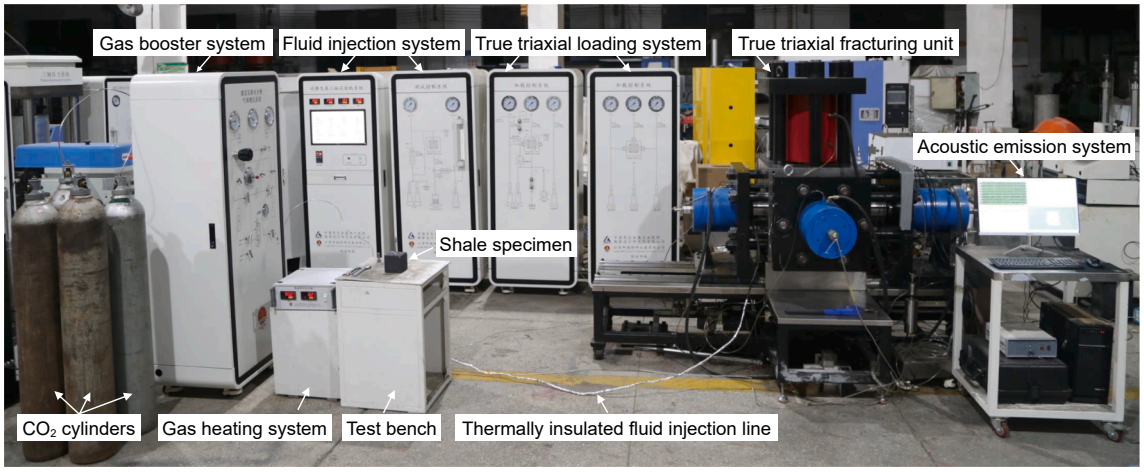


Fig. 3. True triaxial SC-CO_2 rock fracturing test system.

subsequently storing it in the high-pressure storage tank. Two initial pressures were established in the present study: 2 and 8 MPa. The former process enabled CO_2 to undergo phase change and enter the supercritical state during the injection process, while the latter process enabled CO_2 to reach the supercritical state directly in the high-pressure storage tank. By using the gas heating device, the high-pressure storage tank was heated at 90 °C for 3 h to ensure sufficient heating of the CO_2. In order to reduce heat loss during the process of fluid injection, the injection pipelines were heated with a strip heater and wrapped layer by layer with tinfoil and insulating tape. In addition, a pressure sensor was installed within the high-pressure storage tank. The function of this sensor was to record the injection fluid pressure in real time during the test. The plunger pump used in this study was a dual-cylinder design, capable of maintaining a constant flow rate during fluid injection. (2) The true triaxial stress loading system was composed of three plunger pumps, which could realize stress loading in three directions, with a maximum loading stress of 50 MPa in each direction. (3) The AE monitoring system mainly included AE probes, preamplifiers, a signal analyzer, and a data acquisition device, among which the AE probes were installed in a customized mold behind the pressure plate. This system could apply true triaxial stress to rock samples, while realizing the generation and injection of SC-CO_2, and monitoring the AE signals of rock samples during the fracturing process.

2.3. Fracturing experiment scheme and procedures

In order to explore the potential of SC-CO_2 in enhancing shale gas development, this study set three key parameters: fluid type,

Table 1
Experimental scheme for SC-CO_2 fracturing of shale specimens under true triaxial stress conditions.

Specimen number	Bedding inclination (β), °	Fluid type	Triaxial stress ($\sigma_v/\sigma_H/\sigma_h$), MPa	Horizontal stress difference ($\sigma_H-\sigma_h$), MPa	Injection rate, mL/min
S1	0	water	14/12/10	2	10
S41	0	SC-CO_2	14/12/10	2	40
S39	90	water	14/12/10	2	10
S33	90	SC-CO_2	14/12/10	2	40
S50	0	SC-CO_2	14/12/12	0	40
S43	0	SC-CO_2	14/12/8	4	40
S44	0	SC-CO_2	14/12/6	6	40
S46	0	SC-CO_2	14/12/4	8	40
S47	0	SC-CO_2	12/14/10	-	40

geo-stress conditions, and bedding inclination. The fracturing test scheme was outlined in Table 1. It should be noted that, for the shale specimen at $\beta = 90°$, the minimum principal stress direction was uniformly set parallel to the bedding plane during the sample loading process. According to the test scheme, the experimental procedures of this study were as follows:

(1) Heating process: to bring CO_2 into the supercritical state, both its temperature and pressure must reach the above critical values simultaneously (i.e., ambient temperature above 31.1 °C and pressure above 7.38 MPa). Therefore, in laboratory fracturing tests, both the test pipelines and specimens were preheated. Shale specimens were placed in a heating box and heated at 60 °C for 12 h. The gas heating device and pipeline heating were turned on 12 h before the experiment, with the gas heating device set to 60 °C. Additionally, preheating of specimens and activation of the gas heating device were not required for water fracturing tests.
(2) Loading process: in SC-CO_2 shale fracturing experiments, to reduce heat loss from specimens, preheated rock samples were quickly loaded into the triaxial cell, and injection pipelines were connected. Subsequently, the stress servo software was operated to first load the triaxial stress of the specimens to the target value of the minimum principal stress, followed by sequential application of the intermediate and maximum principal stresses to their respective target values.
(3) Fracturing process: after all the triaxial stresses reached the target values, a plunger pump was used to inject fluid at a constant rate, and AE monitoring was activated simultaneously. The pump was shut down after the pressure dropped rapidly, and test data were saved. It was worth noting that, based on previous studies and preliminary tests in this study, the width of fractures induced by SC-CO_2 fracturing in shale was extremely small, typically ranging from 1 to 50 μm (Li and Zhang, 2019). Currently, SC-CO_2 has poor proppant-carrying capacity due to the lack of suitable viscosifiers (Zheng et al., 2024; Sun et al., 2025), making it difficult to obtain the 3D morphology of fractures. Therefore, to appropriately increase fracture width without altering the original fracture morphology, a small amount of 140-mesh ceramic sand proppant was pre-added into the fracturing hole before the test. After the fracturing test, the triaxial stress was first unloaded via the stress servo system. Then, after replacing the injection pipeline, the injection system was controlled to inject fracturing fluid containing 1% guar gum into the specimen at a constant pressure of 1 MPa for 1 min. After injection, the fractured specimens with appropriately widened fractures were subjected to CT scanning.

3. A methodology for 3D fracture characteristics analysis via U-Net model coupled with CT technology

3.1. A methodology for 3D fracture reconstruction

3.1.1. Reasons for using U-Net model coupled with CT technology to identify fractures

CT scanning enables the comprehensive acquisition of the 3D spatial information of fractures within a sample in a non-destructive manner. To investigate the characteristics of fracturing fractures in shale specimens after fracturing, this study employed an advanced micron-scale CT scanning system to scan the fractured shale specimens. However, the relatively large thickness and density of the shale specimens used in the fracturing tests resulted in a reduction in the resolution of CT scanning images. The voxel resolution of CT scans in this study was approximately 53 μm. The fracture width of the shale specimen was moderately enlarged without altering its original fracture morphology, whereas the width remained small after enlargement. When performing traditional threshold segmentation on CT slice images, the thresholds for pores and fractures in the specimen were found to be extremely close, thereby complicating the effective extraction of fractures. Furthermore, the presence of minute fractures may be obscured by the threshold of the rock matrix, resulting in inaccuracies in fracture extraction.

With the rapid development of deep learning methods, the U-Net model has performed excellently in image segmentation tasks in the medical field, achieving numerous significant results (Yeung et al., 2023). Therefore, to address the difficulty in 3D reconstruction of minute fractures, this study introduced the U-Net model to process CT slices, enabling the construction of more realistic and reliable 3D fracture models. As shown in Fig. 4, the U-Net model adopted a “U-shaped” network structure, consisting of two parts: an encoder and a decoder (Ronneberger et al., 2015). The encoder was mainly used for downsampling the image to extract deep features of the image; the decoder was mainly used for upsampling to restore the extracted deep features into an image for representation. Moreover, after each upsampling, feature fusion was performed with the corresponding downsampling results, ensuring that the feature maps of each layer could effectively participate in subsequent calculations and improving the accuracy of the final prediction results. After a single image is processed by the encoder and decoder, a segmentation prediction map of the target can be generated; subsequently, this prediction map (corresponding to predicted values) and the label map (corresponding to true values) were input into the loss function for calculation to obtain the corresponding loss value, thus completing the forward propagation process of a single image (Tian et al., 2025). Then, the Adam gradient descent algorithm was used to approximate the loss function value to the minimum (Kingma and Ba, 2014), and

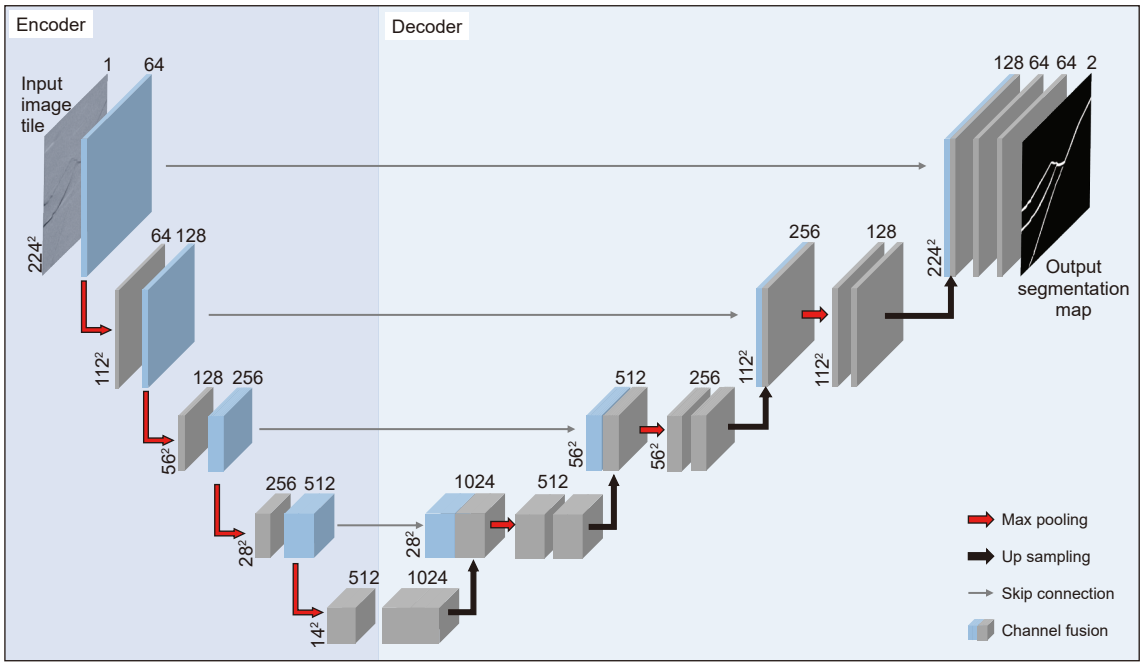


Fig. 4. Schematic diagram of the U-Net architecture.

the error gradient was backpropagated through the back-propagation algorithm to update the model weights (Rumelhart et al., 1986), thereby realizing the backward learning process of a single image. After multiple rounds of iterative learning, the loss value will eventually converge, and the similarity between the prediction map and the label map will gradually increase, thus achieving the target segmentation task. The steps for using U-Net to identify minute fractures in CT slices can be divided into three steps: (I) Data construction; (II) Model training; (III) Performance evaluation. The subsequent sections would provide a detailed introduction to these steps.

3.1.2. Dataset construction

Deep learning models require large datasets for iterative training to acquire the ability to accurately identify fractures. The dataset largely influences the accuracy of fracture identification by the model. Abundant fracture images and precise label maps could improve the identification performance of deep learning models. In this study, image segmentation and data augmentation were performed on CT slices, and label maps for minute fractures were drawn using a point-by-point labeling method, thereby constructing a dataset of extremely fine fractures to meet the training requirements of the deep learning model. The specific steps for constructing the dataset were as follows:

(I) Fiji software was used to export CT slices of shale specimens, and 163 CT slices with extremely fine fractures were selected as typical images;

(II) Each of the 163 original large images was segmented into small images with a size of 224 pixels × 224 pixels, and only the small images containing extremely fine fractures were retained, thus initially establishing an original image library containing 2080 small images;

(III) Labelme software was used for fine labeling of fractures in the original image library, resulting in 2080 label maps that can reflect fracture characteristics. Among them, fracture regions were labeled in white, and non-fracture regions in black. These label maps, together with the original images, constitute the basic dataset. To enhance the credibility of the minute fracture annotation results in the dataset, a consistency verification was performed on the annotations from three independent annotators using the Fleiss' Kappa coefficient, which was one of the most common indices to quantify the agreement with multiple raters (Fleiss et al., 2003). The consistency of the annotation results was determined by evaluating both the label information (i.e., fracture or matrix) and location information of each pixel. Ultimately, the calculated Fleiss' Kappa coefficient reached 0.72. This result demonstrated that the annotation outcomes of different annotators for the same target were highly consistent, indicating that the annotation results in this study were relatively objective and accurate.

(IV) In order to enhance the diversity of the dataset, images in the basic dataset were subjected to data augmentation, yielding a total of 20,800 images. The data augmentation strategies included random flipping, random rotation, random scaling, and random contrast adjustment. Specifically, random flipping referred to horizontal or vertical flipping of the images; random rotation was configured to rotate the images within the range of 0°–180°; the scaling factor was set to vary the image size from 0.5 to 2 times the original dimensions; and the contrast was randomly adjusted within a range of 0.85–1.15 times the original contrast level. These augmentation operations were then applied to the original images via permutation and combination. Finally, a training set containing 16,640 images and a validation set containing 4160 images were established, where the training set was used for model training and the validation set for hyperparameter optimization.

3.1.3. Model training

Once the dataset was constructed, training could be initiated using the U-Net model. Considering that the pixel proportion of

fractures in rock fracture images was generally low, the fracture segmentation task could be categorized as a class imbalance problem. Therefore, the Cross-Entropy loss function (L_{CE}) was combined with the Dice loss function (L_{Dice}) to train the U-Net model. The hybrid loss function (L_{total}) could be expressed as (Li et al., 2024).

$$\begin{cases} L_{CE} = -\dfrac{1}{N}\sum_{i=1}^{N}\sum_{c=1}^{C} y_{i,c}\log\left(p_{i,c}\right) \\ L_{Dice} = 1 - \dfrac{1}{C}\sum_{c=1}^{C}\dfrac{2\sum_{i=1}^{N}\left(p_{i,c}y_{i,c}\right)}{\sum_{i=1}^{N}p_{i,c} + \sum_{i=1}^{N}y_{i,c}} \\ L_{total} = L_{CE} + L_{Dice} \end{cases} \tag{1}$$

where N is the total number of instances; i iterates over each pixel; C is the number of categories; c is the current category; $y_{i,c}$ uses a one-hot encoding scheme corresponding to the ground-truth labels; $p_{i,c}$ represents the predicted output generated by the model for each category.

Following extensive hyperparameter tuning, the optimal hyperparameter configuration that delivered the best training performance was identified. The U-Net model was trained for 300 epochs with an initial learning rate of 0.0005 and a batch size of 16, using the Adam optimizer (Kingma and Ba, 2014). The learning rate was reduced by 50% each time the validation loss remained stagnant over 10 consecutive epochs (Tang et al., 2022). The training dataset was randomly shuffled before each epoch to alleviate batch sampling order bias, enabling the model to capture generalized fracture features. As illustrated in Fig. 5, with the increase in the number of epochs, the loss values of both the training and validation sets exhibited a rapid declining trend and ultimately converged to stable values. These results demonstrated that the model could effectively capture and reconstruct the deep semantic features in the images, thus indicating satisfactory training performance.

3.1.4. Performance evaluation

To enable the U-Net model to capture the morphological features of minute fractures, both original and data-augmented images were incorporated into the training and validation sets. However, it was important to note that the objectivity of the evaluation results may be compromised if the original and data-augmented images were also included in the test set. In order to directly reflect the performance of the model in real applications, an additional 30 representative original CT slices were randomly selected as the test set. After that, manual fracture annotation was performed on the original CT slices to generate reference images, which served as the definitive benchmark for evaluating algorithm recognition performance. Subsequently, a series of comparison tests were conducted using the following methods: interactive thresholding segmentation, edge detection algorithm, and U-Net model. Finally, the performance of these models in recognizing minute fractures was evaluated by four quantitative metrics: precision, recall, dice score, and Intersection over Union (IoU). The formulations of these metrics are provided below (Pham et al., 2023; He et al., 2024).

$$\begin{cases} \text{Precision} = \dfrac{TP}{TP + FP} \\ \text{Recall} = \dfrac{TP}{TP + FN} \\ \text{Dice score} = \dfrac{2TP}{2TP + FP + FN} \\ \text{IoU} = \dfrac{TP}{TP + FP + FN} \end{cases} \tag{2}$$

where TP, FP and FN are true positive, false positive and false negative areas, respectively.

Table 2 presents the visual qualitative evaluation of the performance of various algorithms in identifying minute fractures in CT slices. It can be concluded that, for minute fractures in low-resolution CT slices, interactive thresholding segmentation methods were susceptible to incorrectly identifying metal artefacts, drill holes, and background noise as fractures due to the minute difference in grey scale. The edge detection algorithm also encountered issues such as the inability to completely recognize minute fractures and erroneous identifications. In comparison, the U-Net model applied in this study effectively excluded the effects of most interferences, resulting in relatively complete and accurate identification of minute fractures. To quantitatively evaluate the generalization performance of the model, that is, to accurately obtain the recognition accuracy of minute fractures in images outside the dataset, Table 3 presents a summary of the quantitative evaluation of the recognition effect of various algorithms on minute fractures. It can be observed that, compared to the interactive thresholding segmentation method and edge detection algorithm, the U-Net model achieved the highest scores in various indicators. Overall, the U-Net model exhibited good recognition results, and possessed the ability to accurately identify minute fractures in low-resolution CT slices. Subsequently, the batch-identified CT images were used for 3D reconstruction and digital quantitative analysis of the fractures.

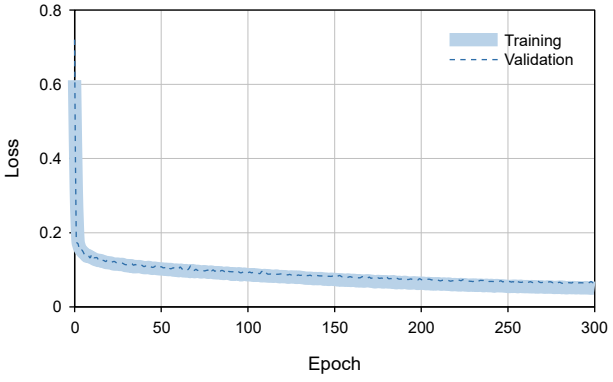


Fig. 5. Loss results of the training and validation phases for the U-Net model in this study.

3.2. An analytical method for 3D fracture characteristics

A thorough analysis of the fracture characteristics of fracture surfaces could facilitate a more comprehensive understanding of the hydrocarbon transport capacity of fractures. Generally, using a 3D laser scanner to obtain point cloud data of fracture surfaces was an effective method for fracture characteristics analysis. However, some post-fracturing specimens contained multiple intersecting fracture surfaces, and some fractures might not penetrate the entire specimen. When using a 3D laser scanner, it was imperative to manually open the fracture surface of the specimen to ensure effective detection. This procedure had the potential to compromise the accuracy of both the surface morphology information and the spatial position information of the fracture surface. Therefore, in this study, point cloud data were obtained from the 3D fracture reconstruction results, and then fracture characteristics were

Table 2
Identification results of minute fractures in low-resolution CT slices via various segmentation algorithms.

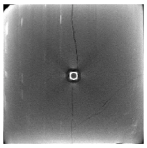
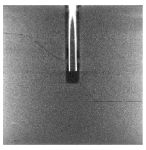
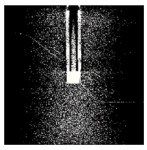
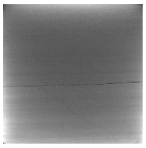
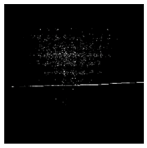
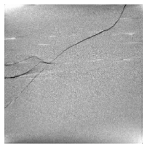
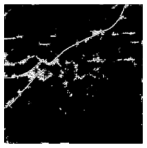
Image sequence	Original CT slices	Reference image	Interactive thresholding segmentation	Edge detection algorithm	U-Net model
1					
2					
3					
4					

Table 3
Quantitative evaluation of the recognition performance of various algorithms for minute fracture identification.

Segmentation algorithms	Precision	Recall	Dice score	IoU
Interactive thresholding segmentation	0.190	0.242	0.213	0.119
Edge detection algorithm	0.273	0.625	0.380	0.235
U-Net model	0.947	0.828	0.884	0.791

analyzed from the point cloud data. The specific steps were as follows: (I) Skeletonization was performed on the identified binarized images containing fractures, i.e., thinning the fracture regions to a single-pixel width while retaining the topological structure of the fractures; (II) 3D reconstruction of the fractures was performed using the processed images, and a meshed surface was generated; (III) Point cloud data of the fracture network were obtained by sampling points on the meshed surface; (IV) The fracture network was segmented to obtain point cloud data of each individual fracture surface. In this study, the area ratio, deviation angle, fractal dimension, and surface roughness were utilized to evaluate the morphological characteristics and complexity of fractures.

3.2.1. Area ratio

The area ratio (AR) can characterize the complexity of a fracture surface. AR is defined as the ratio of the fracture surface area ($A_{surface}$) to the projected area ($A_{projected}$). The calculation is derived from the following formula (Li et al., 2019).

$$AR = \frac{A_{surface}}{A_{projected}} \tag{3}$$

where $A_{surface}$ is calculated by Avizo software based on CT data; $A_{projected}$ is the larger value of the two areas obtained by vertically projecting the fracture surface onto the bottom surface or the side surface of the rock specimen.

3.2.2. Deviation angle

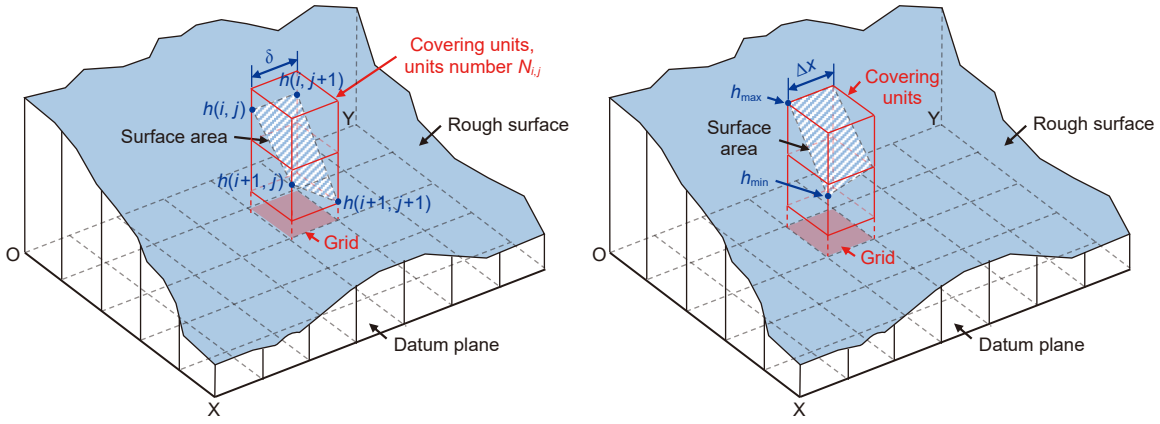
The fracture surface deviation angle (θ) can be quantitatively calculated to characterize the spatial tortuosity of fractures. This can facilitate an in-depth analysis of the factors governing fracture propagation. θ is defined as the minimum angle between the normal vector of the fracture surface and the direction of the maximum principal stress. It can be calculated using the following formula (Yang et al., 2021).

$$\theta = \cos^{-1}\left(\frac{\boldsymbol{n}_f \cdot \boldsymbol{n}_p}{\left\|\boldsymbol{n}_f\right\|\left\|\boldsymbol{n}_p\right\|}\right) \tag{4}$$

where $\boldsymbol{n}_f$ denotes the normal vector of the medial skeleton points; $\boldsymbol{n}_p$ denotes the direction of the maximum principal stress, which corresponds to the positive direction of σ_v in this study. In order to emphasize the minimum spatial deviation of the physically meaningful fracture surface relative to the direction of the maximum principal stress, when $90^\circ \le \theta \le 180^\circ$, the calculated value will be converted to the range of 0° to 90° by taking the supplementary angle.

3.2.3. Fractal dimension

The fractal dimension is considered a reliable metric for quantifying and comparing surface roughness. It has been demonstrated that the fractal dimension is closely related to the irregularity of the surface. Furthermore, the box-counting method, which is characterized by simple mathematical calculation and intuitive physical meaning, is one of the most commonly utilized methods for calculating the fractal dimension. The fundamental concept of this algorithm is to utilize a uniformly spaced grid to cover the entire fractal structure, and subsequently, to determine the number of boxes necessary to achieve this coverage. By changing the box size, the number of boxes under different sizes can be obtained, and the fractal dimension can be calculated based on the trend of the number of boxes as the box size gradually decreases. Fig. 6(a) shows a schematic diagram of the calculation



(a) Calculation principle of fractal dimension (D_f) using the box-counting method.

(b) Calculation principle of the roughness coefficient (R_c) for the fracture surface

Fig. 6. Schematic diagram of the calculation principle for the fracture fractal dimension and surface roughness.

principle of the box-counting dimension method for rough surfaces. A regular cubic grid exists on the XOY plane; in each grid unit with size δ, the four intersection points correspond to the four heights of the fracture surface: $h_1(i, j)$, $h_2(i, j+1)$, $h_3(i+1, j)$, $h_4(i+1, j+1)$. Obviously, when covering this shaded area with cubic boxes of side length δ, the number of cubes ($N_{i,j}$) required to cover the shaded area is determined by the maximum difference between the above four height coordinates. Therefore, the specific calculation formula for $N_{i,j}$ is as follows (Ai et al., 2014).

$$N_{i,j} = \mathrm{INT}\left\{\delta^{-1}\left[\begin{array}{l}\max(h_1(i,j), h_2(i,j+1), h_3(i+1,j), h_4(i+1,j+1)) \\ -\min(h_1(i,j), h_2(i,j+1), h_3(i+1,j), h_4(i+1,j+1))\end{array}\right] + 1\right\} \tag{5}$$

where INT is the integer function, whose function is to round down a real number to the nearest integer. Further, the total number of cubes ($N(\delta)$) required to cover the entire rough surface is:

$$N(\delta) = \sum_{i,j=1}^{n-1} N_{i,j} \tag{6}$$

where n is the number of measurement points on each edge, and satisfies $1 \le i, j \le n-1$. Finally, the fractal dimension (D_f) of the entire fracture surface is calculated by the following formula:

$$D_f = -\lim_{\delta \to 0} \frac{\ln N(\delta)}{\ln(\delta)} \tag{7}$$

3.2.4. Surface roughness

To better describe the detailed morphological characteristics of rough surfaces, the surface roughness coefficient (R_c) is used to quantify the roughness of each fracture surface in the specimen. Fig. 6(b) shows a schematic diagram of the calculation principle for surface roughness. This calculation method is based on the 2D root-mean-square roughness coefficient and uses a 3D form of surface roughness that can characterize the 3D height fluctuations of fracture surfaces (Gadelmawla et al., 2002). This algorithm has the advantages of simple concepts and high calculation accuracy. A larger R_c value indicates greater fluctuations in the fracture surface. The specific calculation formula for R_c is as follows (Zhou et al., 2023).

$$R_c = \sqrt{\frac{1}{N_x \cdot N_y} \sum_{i=1}^{N_x} \sum_{j=1}^{N_y} \left(\frac{h_{max} - h_{min}}{\Delta x}\right)^2} \tag{8}$$

where N_x denotes the number of grids in the X-axis direction, and N_y denotes the number of grids in the Y-axis direction; h_{max} denotes the maximum height of the area covered by the (i, j) unit grid on the reference plane XOY, while h_{min} denotes the minimum height; Δx denotes the sampling interval, which is set to 1 mm.

4. Experimental results and analysis

4.1. Influence of fluid type on 3D fracture characteristics of shale

For the shale specimens with horizontal bedding planes ($\beta = 0°$), as shown in Fig. 7(a), when water was used as the fracturing fluid, the injection pressure rose rapidly in the initial stage. The specimen reached the breakdown pressure (36.82 MPa) at approximately 272 s, and the injection pressure immediately dropped to around 3.4 MPa. When SC-CO_2 was used as the fracturing fluid, the injection pressure increased slowly in the initial stage due to the high compressibility of gaseous CO_2. After the injection pressure exceeded 7.38 MPa, CO_2 entered the supercritical state, and the rate of pressure increase accelerated. At an injection time of approximately 1407 s, the specimen reached the breakdown pressure (21.91 MPa), and the injection pressure dropped rapidly. After the specimen failed, a loud sound of instantaneous gas leakage could be heard near the triaxial cell. This occurred because after the rapid drop in injection pressure, the fluid pressure in the fractures quickly fell below the critical pressure, causing the supercritical CO_2 to

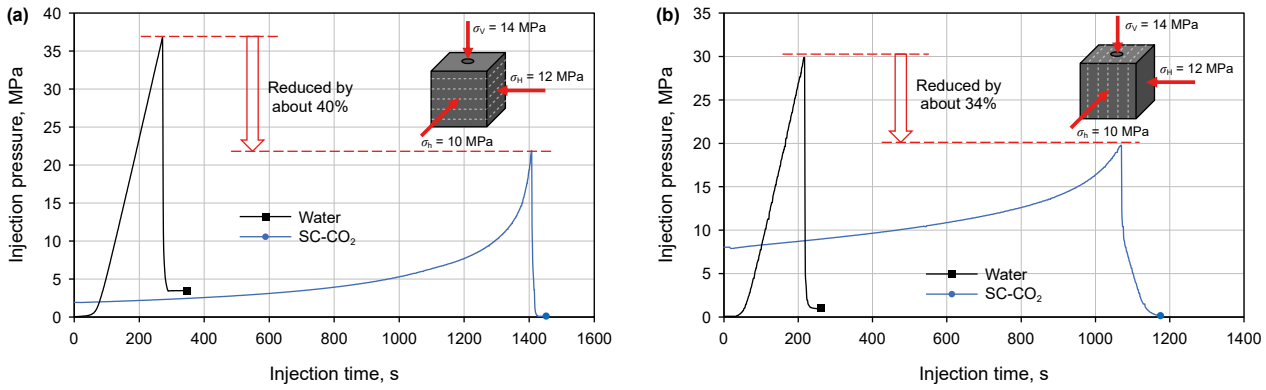


Fig. 7. Injection pressure versus injection time for different fracturing fluids (water or SC-CO_2). **(a)** The shale specimens with $\beta = 0°$ (specimens S1 and S41), **(b)** the shale specimens with $\beta = 90°$ (specimens S39 and S33).

transition into gaseous CO_2. Similarly, Fig. 7(b) shows the fracturing curves of shale specimens with vertical bedding planes ($\beta = 90°$) under different fluid types, and their overall trends are roughly consistent with those of specimens with parallel bedding planes. It should be noted that, to allow CO_2 to reach the supercritical state earlier, the initial injection pressure was increased from 2 to 8 MPa during SC-CO_2 fracturing of this specimen, which reached the breakdown pressure (19.78 MPa) at approximately 1068 s. This indicated that increasing the initial injection pressure could slightly shorten the time required for SC-CO_2 fracturing. In summary, compared with water as the fracturing fluid, SC-CO_2 fracturing reduced the breakdown pressure of shale by approximately 34%–40%, although it required a longer injection time.

In order to elucidate the fracture characteristics and propagation behavior of shale during fracturing with distinct fluid types, Fig. 8 presents the 3D fracture reconstruction of shale specimens with $\beta = 0°$ after fracturing with water and SC-CO_2, respectively. Additionally, the 3D fractal dimension value of the specimen after fracturing is provided above the 3D reconstruction diagram, and the intersecting fracture surfaces are divided into several small fracture surfaces. Herein, the main fracture surfaces formed by water fracturing are called hydraulic fractures (HF); the main fracture surfaces formed by SC-CO_2 fracturing are termed SC-CO_2 fracturing fractures (SCF); and the fracture surfaces roughly parallel to the bedding plane direction are collectively referred to as bedding fractures (BF). As shown in Fig. 8(a1), water fracturing resulted in the formation of three intersecting main fracture surfaces in the specimen. It was observed that the propagation directions of HF_1 and HF_3 initially formed a certain angle with the bedding plane orientation, subsequently gradually shifting to become parallel with the bedding plane, while HF_2 was approximately perpendicular to the bedding plane orientation. From Fig. 8(a2)–(a4), water fracturing initially resulted in the creation of a relatively rough surface near the injected open hole in the specimen, subsequently giving rise to a relatively flat surface at the specimen's edge. This corresponded to water fracturing generating more tensile cracks near the wellbore in the initial stage, and more shear cracks after the fracturing fluid propagated along the bedding plane. As shown in Fig. 8(b1), the process of SC-CO_2 fracturing resulted in the creation of both bedding fractures and fracture surfaces that crossed obliquely through the bedding planes. As demonstrated in Fig. 8(b2)–(b3), the bedding fracture surfaces that formed in proximity to the wellbore still exhibited a certain degree of roughness. Furthermore, the process of SC-CO_2 fracturing was observed to result in the formation of rough surfaces in locations distant from the wellbore. The aforementioned phenomena were consistent with conclusions derived from previous studies that employed AE monitoring techniques. SC-CO_2 fracturing primarily induced more shear cracks during the initial stage of crack initiation, while generating more tensile cracks during the crack propagation stage (Wu et al., 2022).

In the case of shale specimens with vertical bedding planes, as illustrated in Fig. 9(a1), water fracturing resulted in the formation of an inclined primary fracture plane, designated as HF, within the specimen. During the initial propagation phase, the propagation direction of HF formed an angle with the vertical bedding plane. By the late propagation stage, beneath the specimen, the fracture propagation direction gradually shifted to become parallel with the bedding plane. This finding suggested that fractures initially obliquely penetrated the bedding planes during the early propagation stage, subsequently activating a small part of BF in the late propagation stage. However, BF exhibited extremely poor connectivity. As demonstrated in Fig. 9(a2)–(a3), water fracturing yielded a rough surface with a surface roughness of 0.413, while the surface roughness of the incompletely opened bedding planes was minimal at 0.143. It should be noted that the direction of HF was not perpendicular to the direction of minimum principal stress; rather, it was close to perpendicular to the direction of intermediate principal stress. This finding is consistent with the experimental results of previous studies (Abdelaziz et al., 2024). This is because shale is a transversely isotropic material, and fractures in such materials tend to occur along bedding planes, thereby interfering with the control of in-situ stress on fracture direction. As demonstrated in Fig. 9(b1), the process of SC-CO_2 fracturing resulted in the formation of three distinct fracture surfaces in the specimen. Among these, SCF_1 emerged as the main fracture surface, with SCF_2 and SCF_3 acting as branch fracture surfaces. During the initial stage of fracture propagation, SCF_1 obliquely penetrated the bedding plane. In the later phase of fracture propagation, complex interactions occurred at the bedding plane, including deflecting and penetrating. Combined with Fig. 9(b2)–(b4), it can be found that the main fracture surface, designated SCF_1, exhibited a large roughness, with a magnitude of 0.851. This was due to the fact that, in the area distal to the injection open hole, the specimen produced many branch fractures, and the bedding planes BP_1 and BP_2 well connected SCF_1 with some branch fractures, thus rendering these branch fractures part of the SCF_1 surface. In a similar manner, the repeated "deflecting-then-penetrating" interactions that occurred when branch fractures encountered bedding planes led to SCF_2 presenting a stepped curved shape, which resulted in its relatively large roughness, reaching 0.631. Conversely, the roughness of SCF_3 was comparatively minimal, with a value of 0.217.

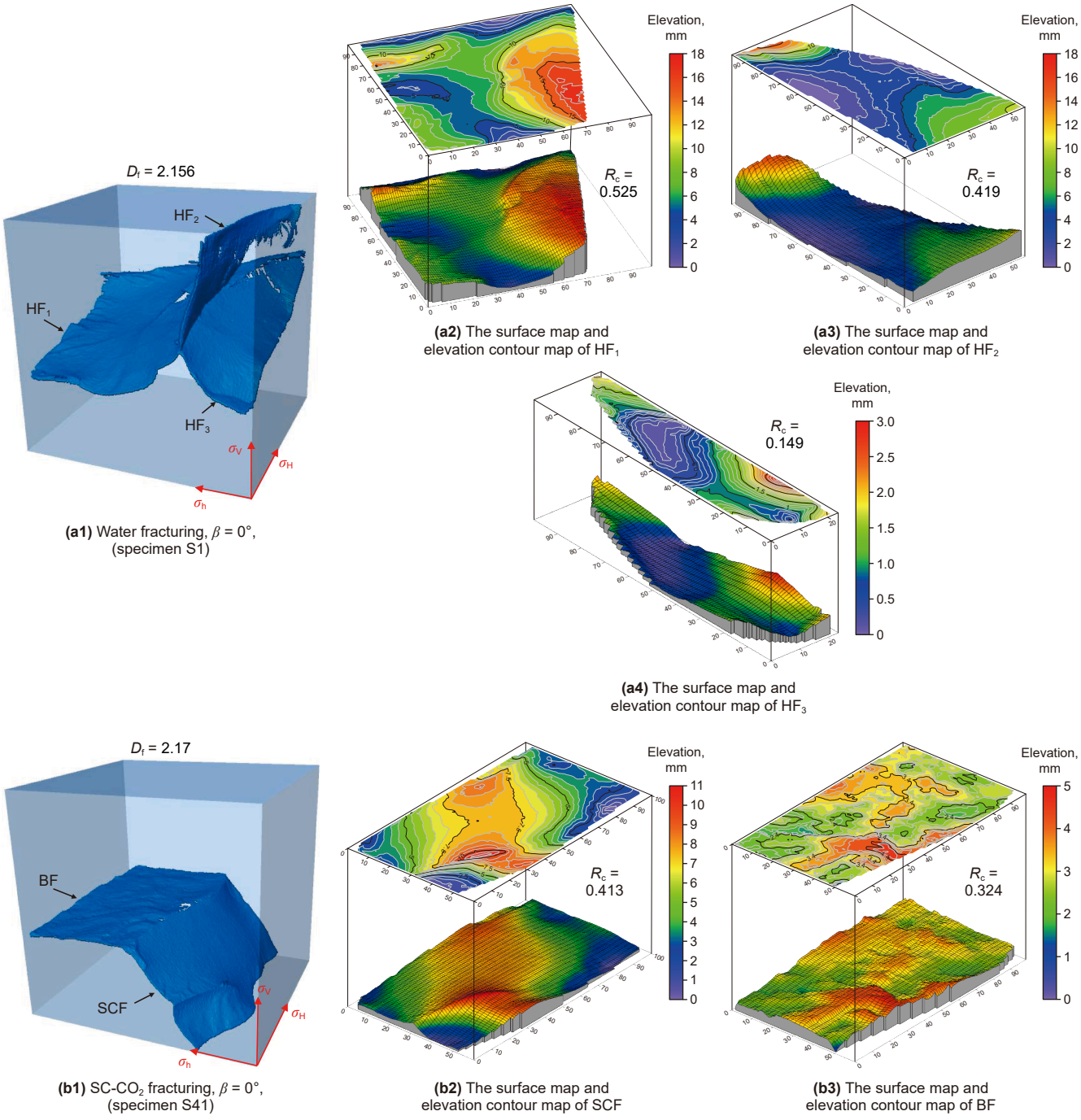
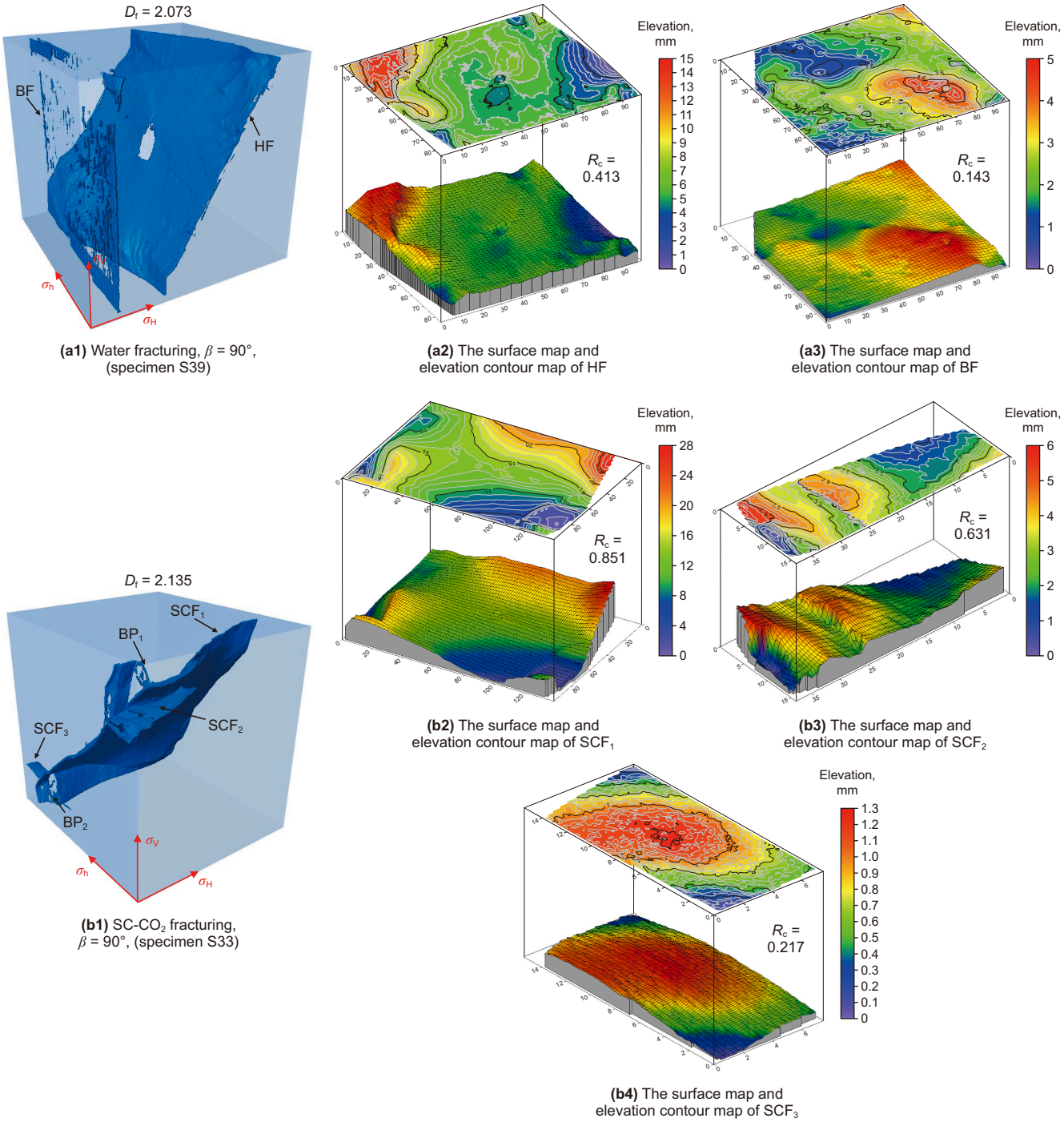


Fig. 8. 3D fracture reconstruction results of shale specimens with $\beta = 0°$ after water or SC-CO_2 fracturing.

As demonstrated in Fig. 10(a) and (c), in comparison with water as the fracturing fluid, the area ratio, fractal dimension and surface roughness of the fracture surface in the $\beta = 90°$ specimen were all enhanced following fracturing with SC-CO_2. In other words, the fractures generated by SC-CO_2 fracturing demonstrated higher levels of roughness and complexity in comparison to those generated by water fracturing. Furthermore, evidence from the 3D fracture surface indicated a correlation between the enhancement of fracture characteristic parameters in the $\beta = 90°$ specimen and the phase transition of CO_2. The energy stored in CO_2 was released intensively when the fracture extended close to the specimen end face, and the phase transition of CO_2 enhanced the driving force for unstable fracture propagation. However, following the fracturing process involving SC-CO_2, the fractal dimension of the fracture surface of the $\beta = 0°$ specimen exhibited only a marginal increase in comparison to water fracturing. Furthermore, the area ratio and surface roughness exhibited a decline. The underlying reason for this phenomenon was that the $\beta = 0°$ specimen formed an opened bedding plane in one side of the specimen due to the effect of SC-CO_2 fracturing. This resulted in the rapid leakage of CO_2 from the bedding plane, thereby hindering the phase transition of CO_2 from amplifying the fracturing effect. Furthermore, as demonstrated in Fig. 10(b), the mean deflection angles of the fracture surfaces of the $\beta = 0°$ specimen were 30.11° and 27.34°, respectively, while those



(a1) Water fracturing, β = 90°, (specimen S39)

(a2) The surface map and elevation contour map of HF

(a3) The surface map and elevation contour map of BF

(b1) SC-CO_2 fracturing, β = 90°, (specimen S33)

(b2) The surface map and elevation contour map of SCF_1

(b3) The surface map and elevation contour map of SCF_2

(b4) The surface map and elevation contour map of SCF_3

Fig. 9. 3D fracture reconstruction results of shale specimens with $\beta = 90°$ after water or SC-CO_2 fracturing.

of the $\beta = 90°$ specimen were 60.13° and 51.04°, respectively. Irrespective of the type of fracturing fluid utilized, specimens with the same bedding inclination demonstrated similar average deflection angles of the fracture surfaces. This finding suggested that, under conditions of minor horizontal geo-stress differences, the effect of bedding inclination on the fracture propagation direction during fracturing appeared to be more significant than that of fluid type.

In a word, the results of 3D fracture reconstruction in this study clearly demonstrated that the ability of SC-CO_2 to activate bedding planes and the phase transition effect of CO_2 were the two core mechanisms responsible for the generation of such rough and complex fractures during SC-CO_2 fracturing. Firstly, the low viscosity and high diffusion capacity of SC-CO_2 enabled it to induce the development of fractures along bedding planes, which could intersect with the primary fracture. Secondly, during fracture propagation, rapid pressure drops inside the fracture drove the instantaneous phase conversion of SC-CO_2 into a gaseous state. This phase transition was accompanied by intense volume expansion, which provided sufficient driving force for the rapid

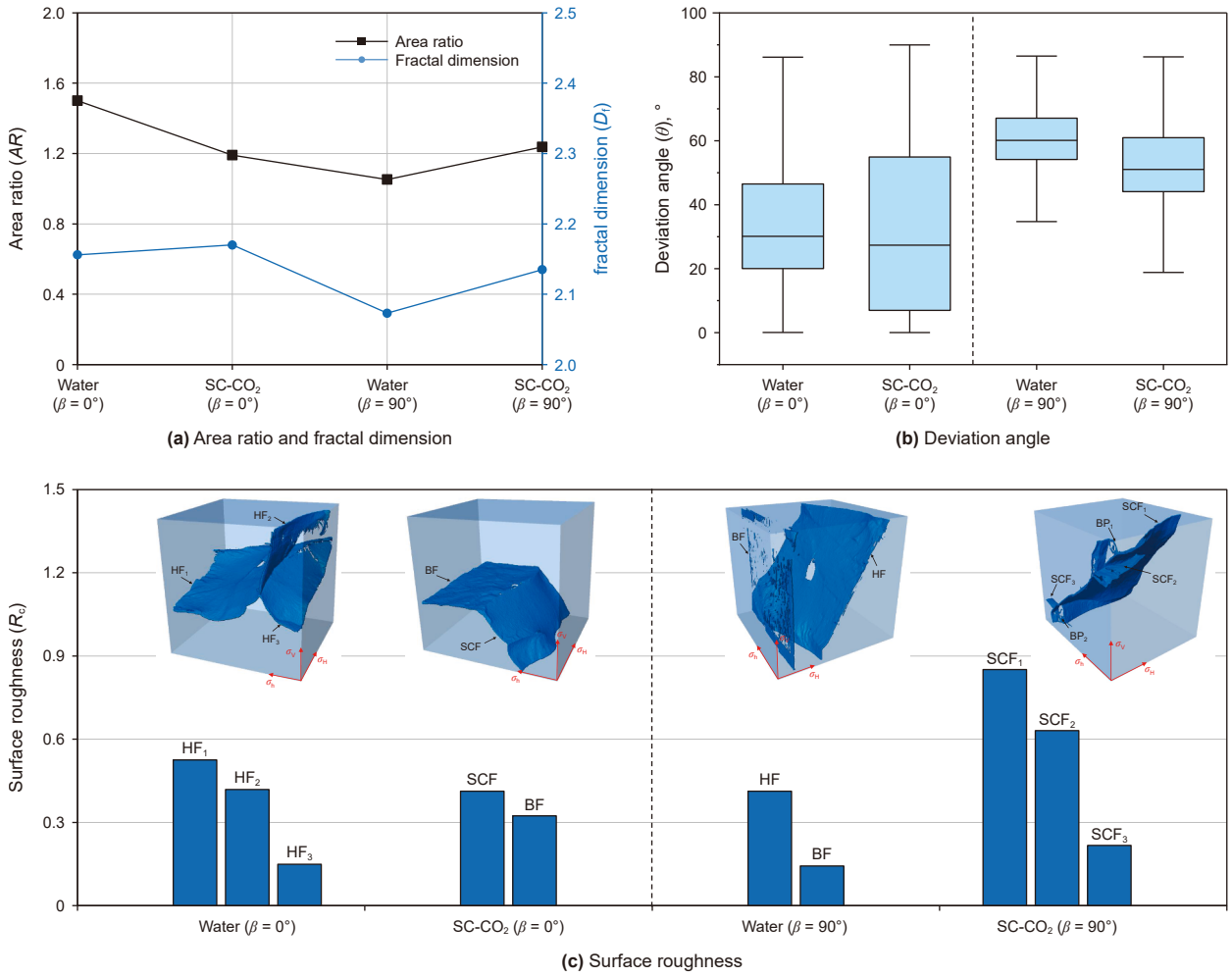


Fig. 10. Digital quantification of 3D fracture characteristics in shale after water or SC-CO_2 fracturing.

and unstable propagation of fractures. However, if SC-CO_2 fracturing activated highly connected weak bedding planes in shale, the CO_2 fluid might leak directly along the opened bedding planes, thereby greatly weakening the enhanced fracturing effect induced by CO_2 phase transition.

4.2. Influence of horizontal stress difference on 3D fracture characteristics of shale

The magnitude and direction of in-situ stress significantly influence the propagation direction and range of fracturing fractures. Therefore, different horizontal stress differences ($\sigma_H - \sigma_h$ = 0, 2, 4, 6, 8 MPa) were set in this study, and the specific scheme can be seen in Table 1.

Fig. 11 shows the SC-CO_2 fracturing curves of shale under different horizontal stress differences. It can be seen that the horizontal stress difference did not significantly affect the overall shape of the fracturing curves of the specimens. As the injection time increased, the injection pressure initially rose gradually and then accelerated rapidly. This was followed by a precipitous decline in pressure once the breakdown pressure was attained. As demonstrated in Fig. 11(a), in the absence of a horizontal stress difference, the AE system detected a substantial number of signals during thefracture initiation stage and fracture propagation stage. This finding indicated that the fracture propagation behavior exhibited obvious staged characteristics at a horizontal stress difference of 0 MPa. However, as illustrated in Fig. 11(b)–(e), when a horizontal stress difference existed, it was only when the injection pressure approached its peak value that a substantial increase in AE energy became evident. This finding indicated that under conditions of a large horizontal stress difference, the formation of microcracks in the specimens was suppressed during the early stages. The energy tended to be released intensively and instantaneously upon the initiation of a macroscopic fracture.

As illustrated in Fig. 12, the 3D reconstruction results of fractures facilitated a more intuitive comprehension of the fracture propagation under varying horizontal stress differences in shale specimens. As shown in Fig. 12(a1)–(a4), when the horizontal stress difference was 0 MPa, the process of SC-CO_2 fracturing gave rise to the formation of three intersecting main fracture surfaces in the specimen. Specifically, the process of SC-CO_2 fracturing opened the weak bedding plane (BF) near the wellbore, and then the fracture surface continued to penetrate the bedding plane obliquely on both sides simultaneously on the basis of this BF, eventually forming two very similar fracture surfaces (SCF_1 and SCF_2) distributed on both sides of the injection open hole. Among them, the surface roughness of SCF_1 and SCF_2 was very close, both around 0.62. As shown in Fig. 8(b1)–(b3), when the horizontal stress difference reached 2 MPa, SC-CO_2 fracturing also opened the weak bedding plane (BF) near the wellbore. However, only one oblique fracture surface (SCF) crossing the bedding plane was formed on the lower side of the injection cavity. As shown in

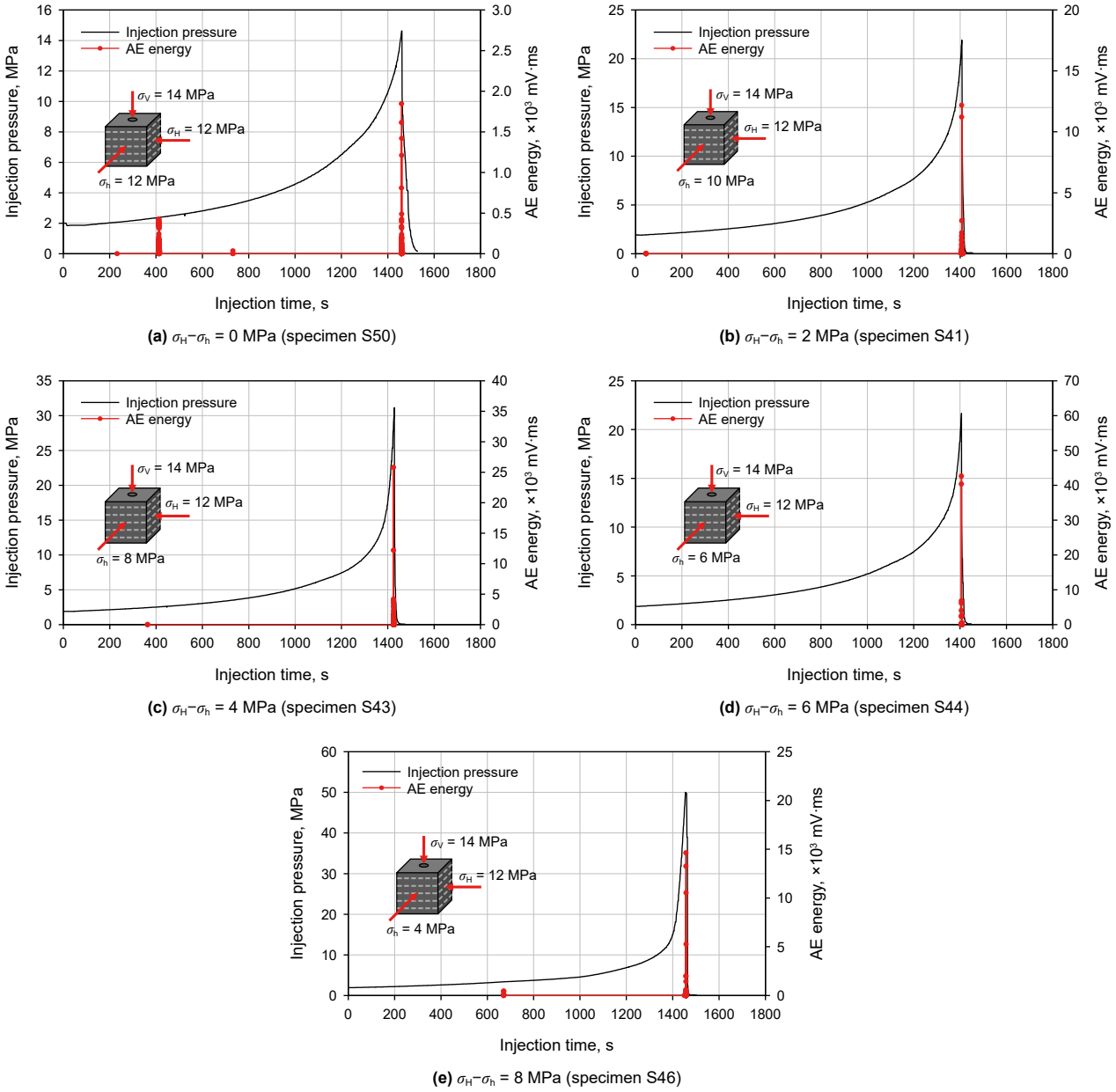


Fig. 11. Variation curves of injection pressure and AE energy with injection time during SC-CO_2 fracturing under different horizontal stress differences.

Fig. 12(b1)–(b5), when the horizontal stress difference increased to 4 MPa, SC-CO_2 fracturing resulted in the formation of one main fracture surface (SCF_1) and three branch fracture surfaces (SCF_2, SCF_3, and SCF_4) in the specimen. The three branch fractures were all distributed near the surface of the specimen. It was noteworthy that the main fracture surface (SCF_1) underwent a deflection towards the upper left during its propagation, which accounted for the relatively high roughness of the fracture surface. In addition, SCF_1 and SCF_2 were connected by an open bedding plane fracture (BF). The generation of numerous branch fracture surfaces in the specimen may be related to the phase transition of CO_2. When the specimen fractured, the volume of SC-CO_2 expanded instantaneously due to the phase transition that occurred during the sudden pressure drop. This violent expansion significantly enhanced the fracture propagation capability at the specimen edges. As shown in Fig. 12(c1)–(c3), when the horizontal stress difference further increased to 6 MPa, SC-CO_2 fracturing generated one main fracture surface (SCF_1) in the specimen and opened one bedding plane (BF) near the specimen surface. It was worth noting that the orientation of SCF_1 began to approach the direction perpendicular to the minimum principal stress. As demonstrated in Fig. 12(d1)–(d2), when the horizontal stress difference further increased to 8 MPa, SC-CO_2 fracturing merely resulted in the formation of a single main fracture surface (SCF) in the specimen. Moreover, the SCF was perpendicular to the direction of the minimum principal stress. In a word, the horizontal stress difference was a key factor regulating the propagation pattern of SC-CO_2 fracturing fractures. Specifically, under low stress difference, SC-CO_2 fracturing tended to open bedding planes first, and then the fracture turned and ran obliquely across the bedding plane. As the horizontal stress difference gradually increased, SC-CO_2 fracturing could still well cross the bedding planes, but its ability to activate bedding planes weakened. Under high stress difference, SC-CO_2 fracturing tended to induce a single

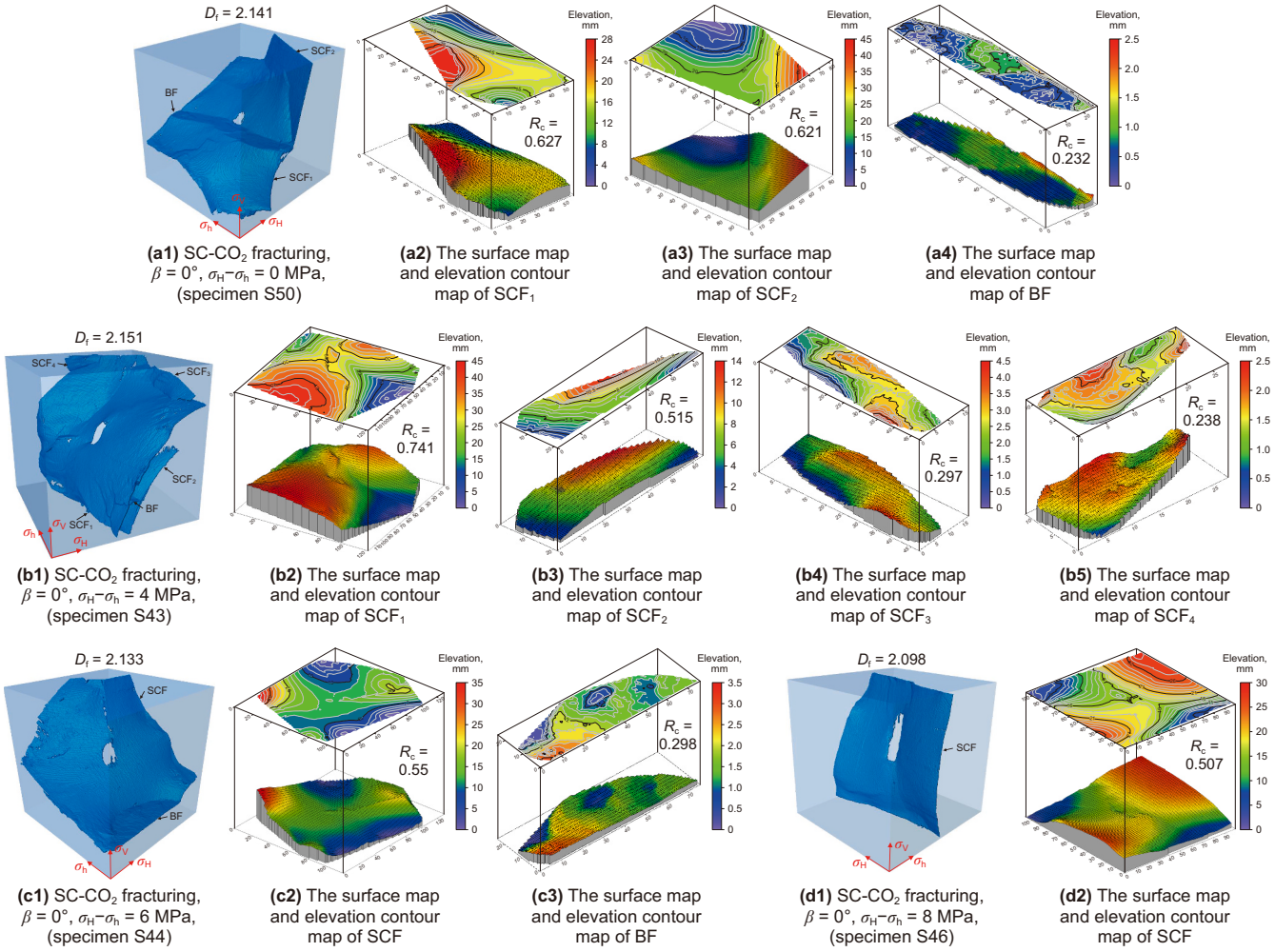


Fig. 12. 3D fracture reconstruction results of shale specimens after SC-CO_2 fracturing under different horizontal stress differences.

main fracture perpendicular to the minimum principal stress in the shale specimen.

By reviewing the relationship between the propagation direction of the main fracture surface and the principal stress direction in this study, it was found that the propagation direction of the main fracture surface was basically consistent with the direction of the maximum principal stress. However, under low horizontal stress differences, the fracture surface was generally not strictly perpendicular to the minimum principal stress direction. This was because the low horizontal stress difference was insufficient to fully control the propagation direction of SC-CO_2 fracturing fractures. At this time, the influence of shale's own structural characteristics (such as bedding planes, natural fractures) and SC-CO_2's low viscosity and high permeability on the fracture propagation direction became more prominent. As the horizontal stress difference gradually increased, the propagation direction of SC-CO_2 fracturing fractures was gradually controlled by the large horizontal stress difference, and the main fracture surface was basically perpendicular to the minimum principal stress direction.

As demonstrated in Fig. 13, as the horizontal stress difference gradually increased, the breakdown pressure of the specimen exhibited an overall upward trend. Combined with the 3D reconstruction results of fractures under different in-situ stress conditions, as the horizontal in-situ stress difference increased, the fracture propagation direction of the specimen was gradually dominated by the stress field. Under the in-situ stress-dominated

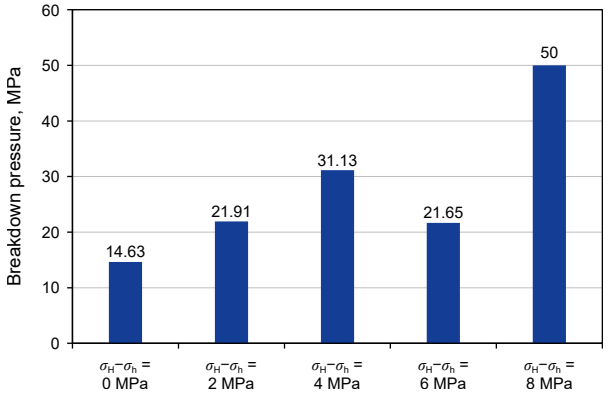


Fig. 13. Relationship between breakdown pressure and horizontal stress difference in SC-CO_2 fracturing tests.

condition, the fractures tended to propagate perpendicular to the minimum principal stress, which in this study meant that the fractures had to penetrate the intact shale matrix vertically. Evidently, fracturing the intact shale matrix requires a much higher injection pressure compared with activating the relatively weak bedding planes. Notably, at a horizontal stress difference of 6 MPa, the propagating fractures encountered weak horizontal

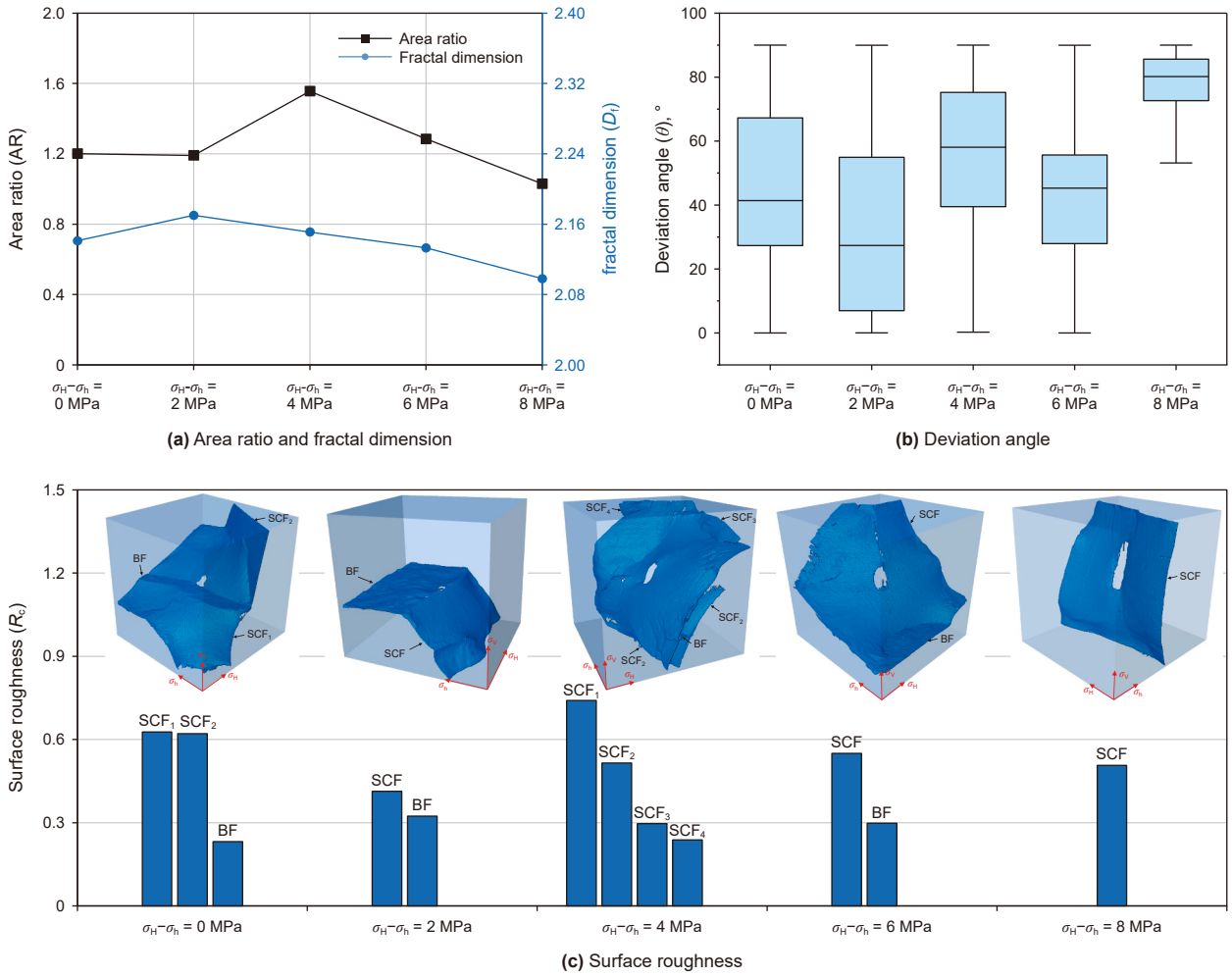


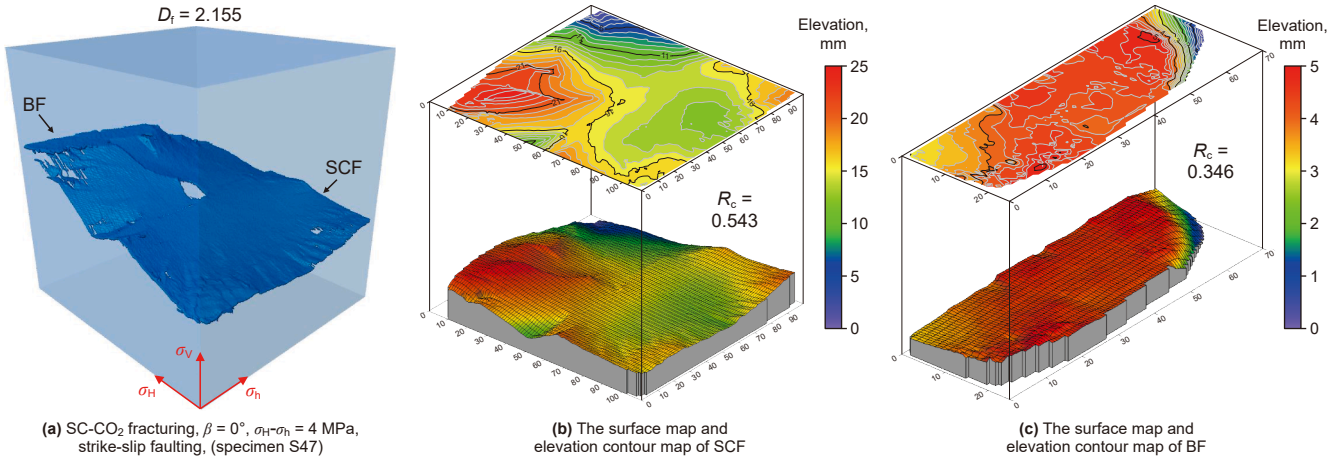
Fig. 14. Digital quantification of 3D fracture characteristics in shale after SC-CO_2 fracturing under different horizontal stress differences.

bedding planes and consequently deflected from their original path. Since the resistance to fracture propagation along the bedding planes was considerably lower than that for fracture propagation through the intact shale matrix, this specimen displayed a marked reduction in breakdown pressure.

As presented in Fig. 14(a) and (c), under conditions of low horizontal stress difference (0, 2, and 4 MPa), the fractal dimension and surface roughness of fractures were relatively high, and the variation trends of various fracture parameters with increasing horizontal stress difference were inconsistent. It seemed that a smaller horizontal stress difference had no significant influence on the fracture parameters. In contrast, when the horizontal stress difference was increased further (6 and 8 MPa), the area ratio, fractal dimension, and surface roughness of the fracture surface simultaneously exhibited a decreasing trend with increasing horizontal stress difference. This finding suggested that a high horizontal stress difference coefficient can reduce the roughness and complexity of fractures induced by SC-CO_2 fracturing. As demonstrated in Fig. 14(b), with the increase of the horizontal stress difference, the mean deviation angle of the specimens exhibited an overall upward trend, which signifies that the fracture propagation direction of the specimens gradually became perpendicular to the direction of the minimum principal stress. This finding indicated that the fracture propagation mechanism of the shale specimens shifted progressively from being dominated by bedding planes to being stress-dominated as the horizontal stress difference increased. It should be noted that the fluctuation in the mean deviation angle was attributable to the presence of horizontal fracture surfaces within the fracture networks of individual specimens. These fracture surfaces exhibited deflection angles close to 0°, thus reducing the overall average deflection angle of the shale specimens.

4.3. Influence of stress regime on 3D fracture characteristics of shale

Two stress regimes were prevalent in shale gas reservoirs, namely normal faulting ($\sigma_V > \sigma_H > \sigma_h$) and strike-slip faulting ($\sigma_H > \sigma_V > \sigma_h$) (Hossain et al., 2000; Zou et al., 2016). To elucidate the influence of stress regimes on the fracture propagation behavior of shale in SC-CO_2 fracturing, two stress regimes were adopted in this study: normal faulting (σ_V = 14 MPa, σ_H = 12 MPa, σ_h = 10 MPa) and strike-slip faulting (σ_V = 12 MPa, σ_H = 14 MPa, σ_h = 10 MPa). As shown in Fig. 8(b1), under the normal faulting stress regime, the SCF of the specimen basically propagated along the direction of the maximum principal stress; however, due to the small horizontal stress difference, the propagation direction was not strictly perpendicular to the direction of the minimum principal stress. As illustrated in Fig. 15(a)–(c), under the strike-slip faulting stress regime, SC-CO_2 fracturing generated a main fracture surface (SCF) in the specimen and opened bedding fractures (BF) near the specimen

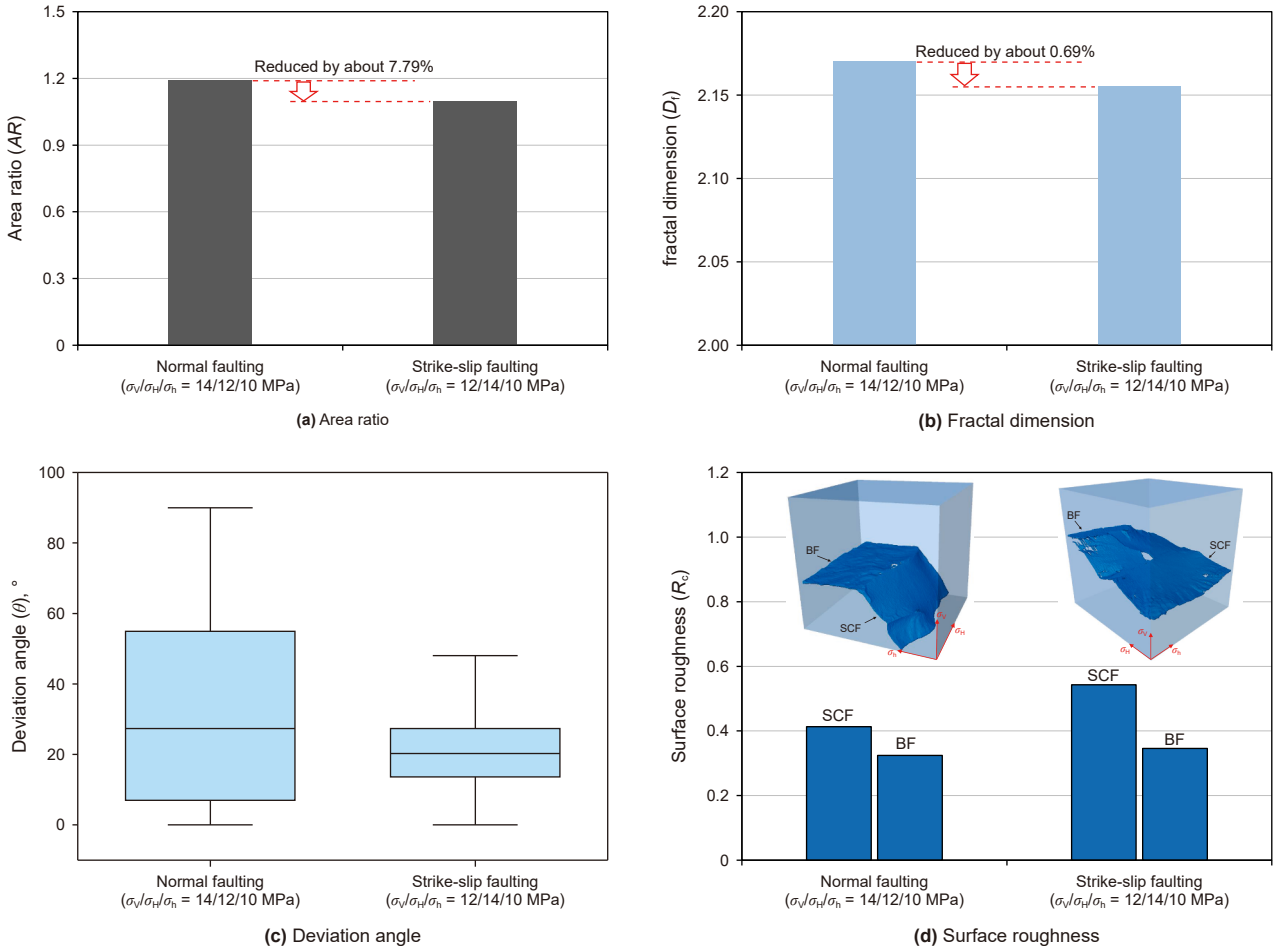


(a) SC-CO_2 fracturing, β = 0°, σ_H-σ_h = 4 MPa, strike-slip faulting, (specimen S47)

(b) The surface map and elevation contour map of SCF

(c) The surface map and elevation contour map of BF

Fig. 15. 3D fracture reconstruction results of shale specimens after SC-CO_2 fracturing under strike-slip faulting stress regime.



(a) Area ratio

(b) Fractal dimension

(c) Deviation angle

(d) Surface roughness

Fig. 16. Digital quantification of 3D fracture characteristics in shale after SC-CO_2 fracturing under different stress regimes.

edge. σ_H became a key driving factor, guiding the fractures to propagate along its orientation.

As demonstrated in Fig. 16(a) and (b), the area ratio and fractal dimension of the fracture surface under the normal faulting and strike-slip faulting stress regimes were found to be highly close. As demonstrated in Fig. 16(c), the mean deviation angles of cracks under the normal faulting and strike-slip faulting stress regimes were also relatively close, at 27.34° and 20.24°, respectively. However, under the strike-slip faulting stress regime, the distribution range of θ for the specimens was mainly between 0° and 30°, which was significantly more limited. Furthermore, the fracture surfaces of specimens under the strike-slip faulting stress regime exhibited higher surface roughness values (see Fig. 16(d)). This phenomenon could be attributed to the fact that when the

specimen was under the strike-slip faulting stress regime, the bedding planes were less constrained by σ_V, and multiple layers at the specimen edge were opened, resulting in greater undulations on the fracture surface. In summary, given that the values of the first and second principal stresses differed by a mere 2 MPa in this study, the varying stress regimes exerted minimal influence on the complexity of the fracture network. In conjunction with the 3D fracture surface, it can be determined that the crack propagation direction of specimens under the aforementioned two stress regimes was still significantly influenced by bedding planes.

5. Discussions

5.1. Analysis of acoustic information during laboratory fracturing experiments

In laboratory fracturing tests, AE acquisition equipment was used simultaneously to collect acoustic information generated by fracture propagation during the fracturing process. The acoustic information provided detailed insights into fracture propagation behavior induced by fracturing from another perspective. Fig. 17 shows the variation trend of AE energy with injection time during water fracturing and SC-CO_2 fracturing. It can be observed that the surge in AE energy signals mainly occurred during the stage when the specimens reached the breakdown pressure and rapidly generated fractures. The AE energy signals released during SC-CO_2 fracturing of shale appeared more frequently than those during water fracturing. Moreover, the maximum AE energy of SC-CO_2 fracturing was 62% higher than that of water fracturing. In summary, compared with water fracturing, SC-CO_2 fracturing released more frequent and stronger energy signals, which corresponded to the ability of SC-CO_2 fracturing to form rougher and more complex fractures in the shale specimen.

In order to better understand the mechanism of fracturing fracture propagation, the distribution characteristics of the RA value (rise angle, the ratio of rise time to amplitude) and the AF value (average frequency, the ratio of ringing counts to duration) were analyzed to determine the proportions of tensile and shear microcracks induced by fracturing in shale specimens. In general, a higher AF value and a lower RA value indicate tensile cracks, while a lower AF value and a higher RA value indicate shear cracks. The slope (k) was defined as the ratio of AF to RA. It was evident that the k value would significantly influence the outcomes of crack classification. As demonstrated in Fig. 18, among the k values ranging from 0 to 500, the percentage of shear cracks in each specimen was characterized by two phases, namely rapid growth and slow growth, as the k value increased. As presented in Table 4,

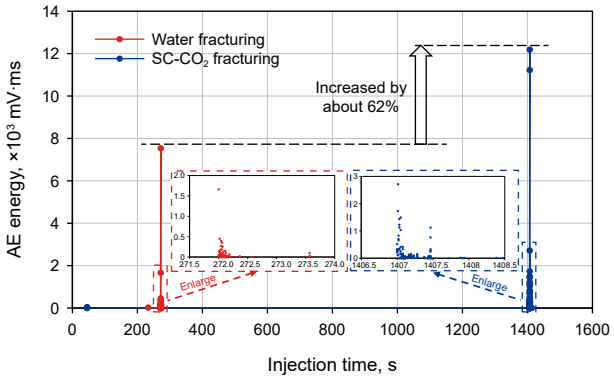


Fig. 17. AE energy versus injection time of shale specimens during water or SC-CO_2 fracturing.

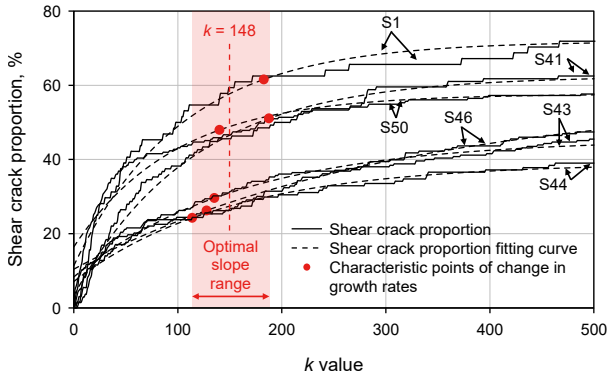


Fig. 18. Variation curves of shear crack proportion with transition line slope.

Table 4
Fitting formulas and fitting effects for variation curves of shear crack proportion with transition line slope.

Specimen number	Exponential decay model	R^2
S1	$y = -60.493902\exp(-x/103.194821)+71.875$	0.9521
S41	$y = -59.199957\exp(-x/114.206686)+62.5$	0.9857
S43	$y = -37.137015\exp(-x/159.119646)+45.490196$	0.979
S44	$y = -31.902439\exp(-x/148.016575)+39.02439$	0.9698
S46	$y = -46.600117\exp(-x/307.884792)+57.042631$	0.9884
S50	$y = -41.196459\exp(-x/96.836027)+57.647059$	0.9436

the single exponential decay model was adopted to describe the relationship between the proportion of shear cracks and the k value, and the fitting effect was good, with a coefficient of determination greater than 0.94. It was noted that there was a critical slope, designated k_0. When the k value fell within the range of 0~k_0, an increase in the k value resulted in a rapid increase in the percentage of shear cracks. This indicated that the k value within this range exerted a greater influence on the results of crack classification. When k exceeded k_0, the percentage of shear cracks exhibited a slow increase, suggesting that after k had surpassed k_0, the influence of the k value on the resultant crack classification was significantly reduced (Wang et al., 2024). Kneedle's algorithm, which was based on the analysis of curvature change, was suitable for identifying the characteristic points in the above fitted curves where the growth rate of k changed from fast to slow (Satopaa et al., 2011). After calculation, the characteristic points were obtained within the range of 114–188 for specimens in this study, with a mean value of 148 (see Fig. 18). Consequently, the optimal transition line between shear and tensile cracks in RA/AF parameter analysis was uniformly determined as 1:148. The crack classification results for each specimen were relatively accurate and could be further analyzed.

Fig. 19 illustrates the proportions of microcracks generated during water fracturing and SC-CO_2 fracturing. Taking shale specimens with horizontal bedding planes as examples (Specimens 1 and 41), the fractures generated by both water fracturing and SC-CO_2 fracturing consisted of tensile cracks and shear cracks, and the proportions of each type exceeded 40%. This indicated that tensile cracks and shear cracks jointly controlled the propagation of fractures induced by fracturing in transversely isotropic materials, which was related to the bedding structure of shale.

As shown in Fig. 11(a), when the horizontal stress difference was 0 MPa, the AE system detected a large number of signals during both the fracture initiation stage and the fracture propagation stage of SC-CO_2 fracturing. Accordingly, the RA/AF parameter analysis method was used to analyze the proportions of

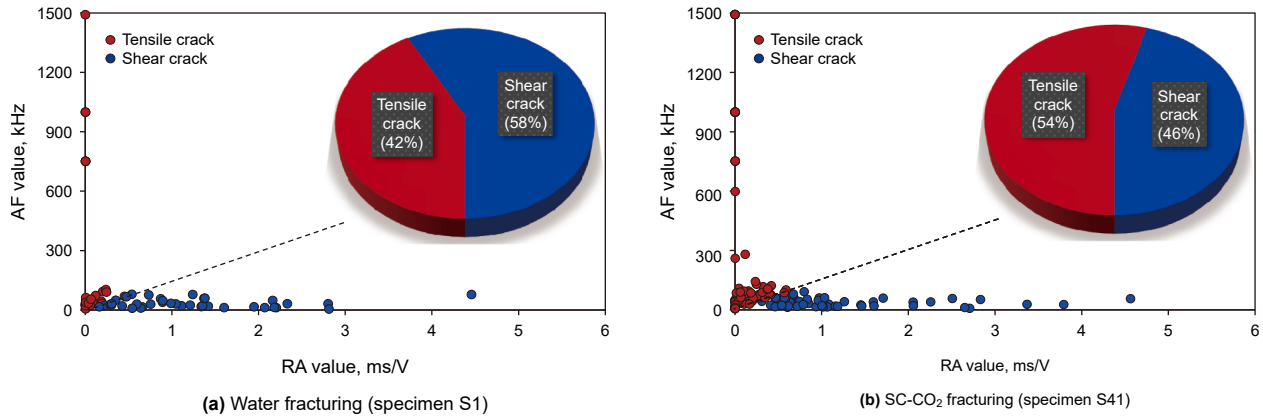


Fig. 19. Proportions of tensile and shear microcracks induced by water or SC-CO_2 fracturing in shale specimens.

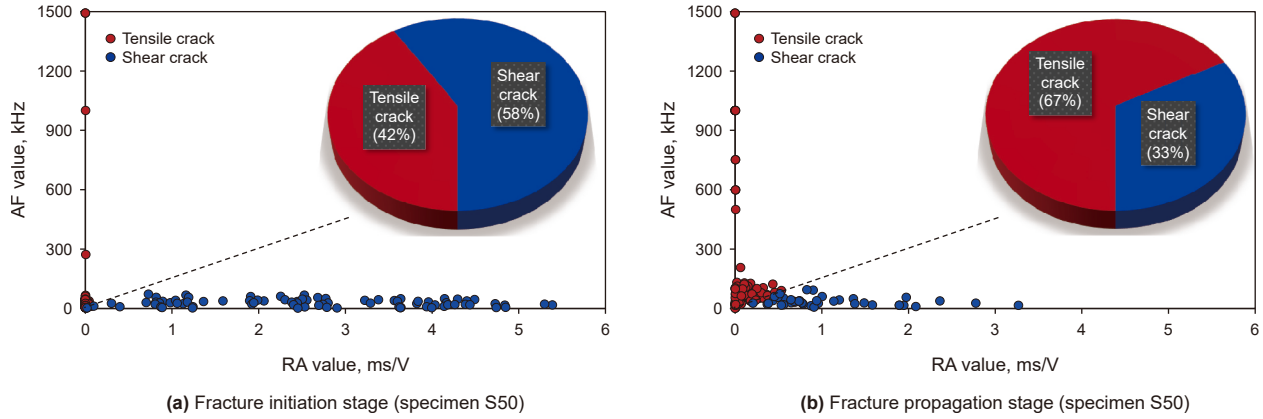


Fig. 20. Proportions of tensile and shear microcracks induced by SC-CO_2 fracturing in shale specimens during the fracture initiation stage and fracture propagation stage.

microcracks generated in these two stages. As shown in Fig. 20(a), during SC-CO_2 fracturing, tensile cracks accounted for 42% of the microcracks generated in the fracture initiation stage, while shear cracks accounted for 58%. This indicated that the initially generated cracks exhibited a mixed tensile-shear type, but shear cracks were predominant. However, as shown in Fig. 20(b), in the fracture propagation stage, the proportion of tensile cracks increased significantly to 67%, while the proportion of shear cracks decreased to 33%. This showed that in the fracture propagation stage, tensile cracks became the main form of microcrack generation. This variation in the proportions of microcracks reflected that during SC-CO_2 fracturing, the fracturing mechanism differed between different stages. The 3D reconstruction results of fractures in this study (see Fig. 12(a1)) provided clear visual evidence to validate the conclusion that, when the horizontal stress difference was 0 MPa, fracture initiation was predominantly induced by shear action, whereas the contribution of tensile action to microcrack formation increased progressively as fracture propagation proceeded. This offered an important basis for the in-depth understanding of the fracture mechanism of shale during SC-CO_2 fracturing. This was consistent with previous findings: viscous fluids tended to generate tension-dominant fractures, while low-viscosity fracturing fluids tended to generate shear-dominant fractures (Ishida et al., 2016).

It should be emphasized that the priority tendency of low-viscosity SC-CO_2 to generate shear-dominant fractures meant that SC-CO_2 had the ability to preferentially open weak bedding planes and enhance fracture intersection. Therefore, the proportion of shear cracks was usually highly positively correlated with the activation of bedding planes. The classification results of internal fracturing microcracks in shale specimens after SC-CO_2 fracturing under different stress regimes strongly supported this conclusion. Fig. 21 shows the proportions of tensile and shear microcracks in shale specimens after SC-CO_2 fracturing under different horizontal stress differences. When the horizontal stress difference was 0 MPa, tensile cracks accounted for 53% and shear cracks accounted for 47%, with a relatively balanced distribution of

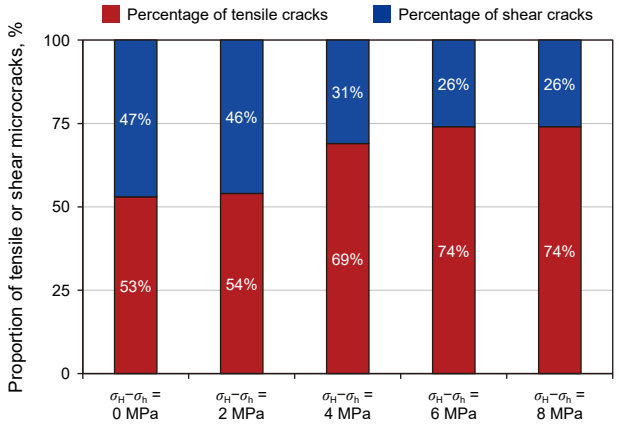


Fig. 21. Proportions of tensile and shear microcracks in shale specimens induced by SC-CO_2 fracturing under different horizontal stress differences.

scatter points corresponding to the two types of cracks in the scatter plot; however, as the horizontal stress difference progressively increased to 2, 4, 6, and 8 MPa, the proportions of tensile cracks successively reached 54%, 69%, 74%, and 74%. It can be concluded that, with the increase of horizontal stress difference, the proportion of tensile cracks inside shale specimens after SC-CO_2 fracturing showed a gradual upward trend. This indicated that the horizontal stress difference had an important influence on the type of microcrack formation in shale during SC-CO_2 fracturing. The larger the horizontal stress difference, the more conducive it was to the generation of tensile cracks, which supported the conclusion of this study that the direction of fracture propagation was dominated by the stress field under a large horizontal stress difference.

5.2. *Fracture propagation patterns when a fracture induced by SC-CO_2 fracturing approached a shale bedding plane*

Many scholars believed that there was a fracture process zone (FPZ) at the front of dynamically propagating fractures (Zhang et al., 2023; Lu et al., 2025). As shown in Fig. 22(a), prior to the intersection of fracturing fractures with bedding planes, three types of microcracks could appear in the FPZ. Crack A was defined as a tensile microcrack generated within the shale matrix when tensile stresses in the FPZ in the fracture height direction exceeded the tensile strength of the shale matrix. Crack B was defined as a shear microcrack on the bedding plane caused by the shear stress in the FPZ in the fracture height direction exceeding the shear strength of the bedding plane. Crack C was defined as a tensile microcrack in the shale matrix caused by the tensile stress in the FPZ in the fracture length direction exceeding the tensile strength of the shale matrix.

Based on the definitions of the three types of microcracks mentioned above, the 3D fracture propagation behavior when encountering bedding planes during SC-CO_2 fracturing can be systematically summarized. As shown in Fig. 22(b)–(e), when a fracture induced by SC-CO_2 fracturing approached a shale bedding plane, four distinct behaviors might occur: (1) activating, (2) deflecting, (3) penetrating, or (4) composite. To be specific, (1) Activating: crack B was preferentially generated on the bedding plane in the FPZ in the fracture height direction, and subsequently, propagation continued in the fracture height direction (crack C). This was manifested by SC-CO_2 injection first activating the bedding plane, followed by fracture propagation in the fracture height direction. (2) Deflecting: as crack C extended to the bedding plane, crack B formed on the bedding plane in the FPZ in the fracture height direction. This manifested as a deflection of the fracture along the bedding plane during its propagation. (3) Penetrating: crack C extended along the fracture length direction, and crack A crossed the bedding plane in the fracture height

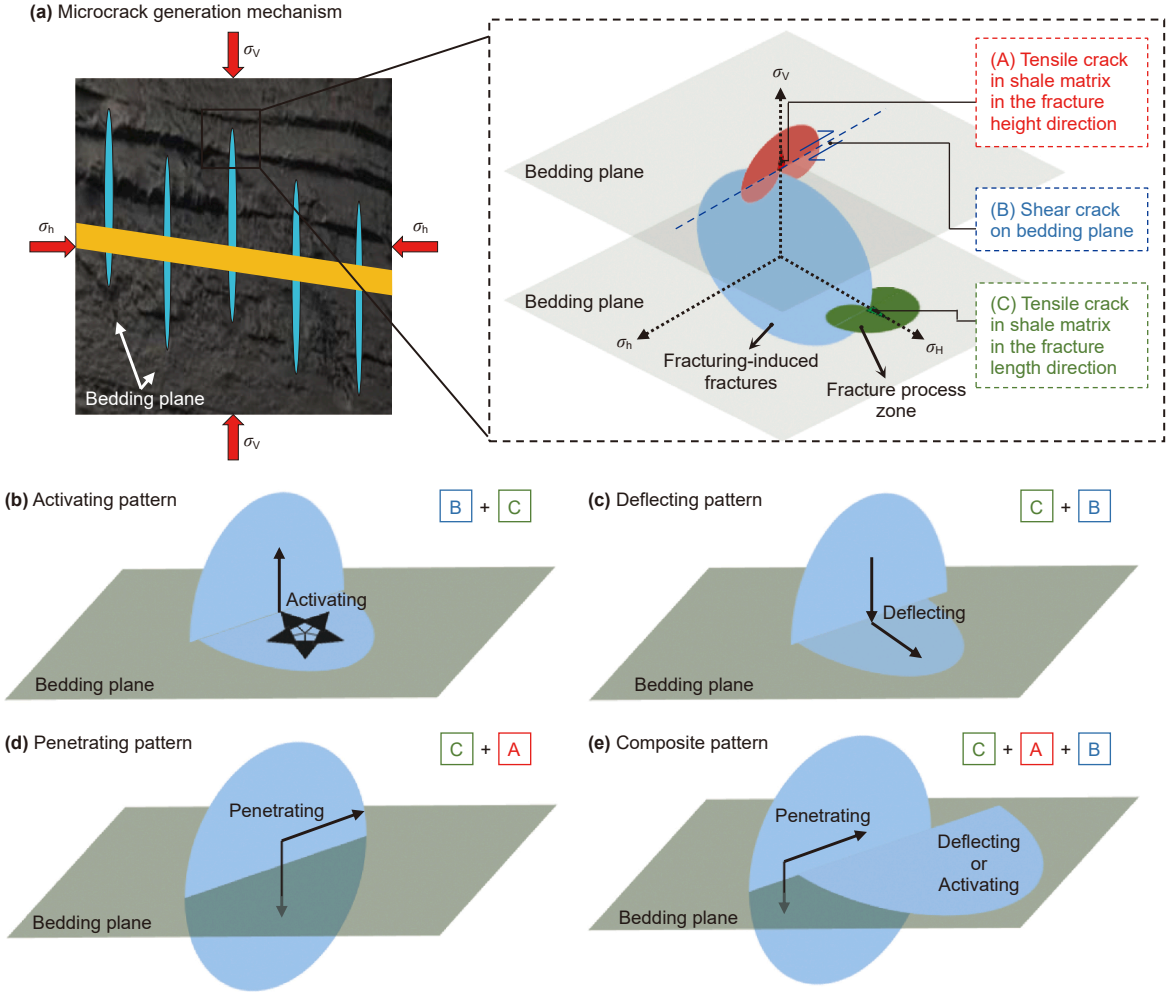


Fig. 22. Schematic diagram of microcrack generation mechanism and fracture propagation patterns when a fracture induced by SC-CO_2 fracturing approached a shale bedding plane (modified from Zhang et al. (2023)).

direction, yet the bedding plane remained stable. (4) Composite: as the conditions for generating cracks A, B, and C were simultaneously satisfied, the crack not only fully penetrated the bedding plane but also opened that bedding plane, either through activation or deflection. This classification of fracture propagation behavior could assist in the evaluation of the propagation characteristics of SC-CO_2 from a 3D perspective.

5.3. Implications

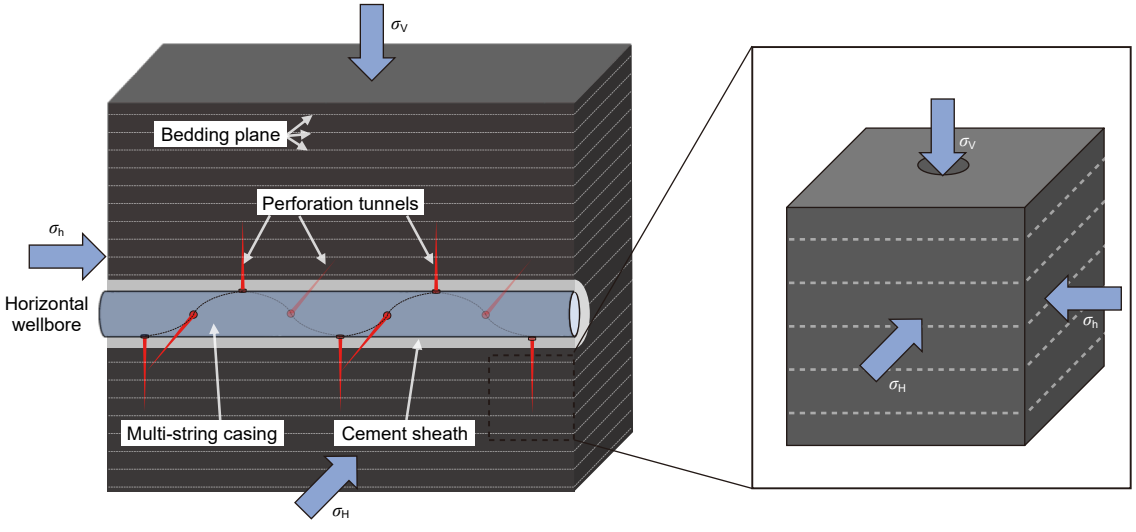
As shown in Fig. 23(a), helical perforation represents the mainstream perforation-fracturing completion method for the stimulation of deep shale reservoirs via hydraulic fracturing. However, the applicability of this perforation technique to shale SC-CO_2 fracturing remains under investigation. Constrained by the limitations of laboratory experimental scales, operations involving casing cementing and helical perforation are difficult to replicate realistically. Consequently, the complex near-wellbore fractures induced by helical perforation were neglected (Tan et al., 2017). Therefore, as illustrated in Fig. 23(b), this study focused on the perforation direction parallel to the vertical principal stress (σ_V), and the analysis of its SC-CO_2 fracturing stimulation effect can provide insights for engineering practices.

The Changning Block in southern Sichuan is a pivotal shale gas production area in China. Based on the measured stress data from six exploration wells, the horizontal in-situ stress difference coefficient in this block ranges from 0.08 to 0.24 (Jin et al., 2024). The in-situ stress difference coefficient is a key parameter for predicting the fracturing stimulation effect of shale reservoirs. It is defined as the ratio of the horizontal stress difference to the minimum horizontal principal stress. A smaller value of this parameter indicates a stronger capacity of the formation to develop a complex fracture network after fracturing; conversely, a larger value leads to more unidirectional fracture propagation, resulting in poor reservoir stimulation effectiveness. Nevertheless, due to the significant spatial heterogeneity of the tectonic stress field in shale reservoirs (Liu et al., 2020), the actual geo-stress conditions may vary considerably between different wells and at different burial depths (Zhang et al., 2017). To cover a broader range of horizontal in-situ stress difference scenarios, the horizontal stress difference coefficients designed in the experiments of this study were 0, 0.2, 0.5, 1.0, and 2.0. The results of this study indicated that under low stress difference coefficients (0 and 0.2), SC-CO_2 fracturing not only opened the shale bedding planes but also formed oblique main fractures in the shale matrix. Under moderate stress difference coefficients (0.5 and 1.0), SC-CO_2 fracturing still generated oblique main fractures in the shale matrix, but its ability to preferentially activate bedding planes was weakened, with bedding plane initiation tending to occur at the edge of the specimen. Under a high stress difference coefficient (2.0), SC-CO_2 fracturing produced main fractures approximately perpendicular to the minimum principal stress in the shale specimen.

Based on the above experimental results, engineers can optimize the SC-CO_2 fracturing scheme according to the actual distribution of in-situ stress difference coefficients in the shale reservoir. Specifically, for fracturing intervals with low to moderate in-situ stress difference coefficients, the number of perforation clusters in the interval can be appropriately increased to promote the formation of complex fracture networks in the reservoir. However, it should be noted that due to the strong diffusion ability of SC-CO_2, rapid filtration loss of SC-CO_2 along the opened bedding planes was observed in the experiments. In actual fracturing operations, the injection rate of SC-CO_2 can be appropriately increased to utilize this filtration effect, activate natural fractures as much as possible, and expand the stimulated reservoir volume. For fracturing intervals with high in-situ stress difference coefficients, the directional penetration advantage of the main fractures should be fully utilized to increase fracture height during reservoir stimulation. Meanwhile, the perforation density should be appropriately reduced to mitigate filtration loss of SC-CO_2, thereby ensuring successful fracture initiation. In addition, the experimental data of this study showed that the higher the in-situ stress difference coefficient, the higher the corresponding reservoir breakdown pressure tended to be. Therefore, to avoid the risk of overpressure operation of CO_2 fracturing pump trucks, it is imperative to conduct full-process pump pressure monitoring during the construction of fracturing intervals with high in-situ stress difference coefficients.

5.4. Limitations

This study has two main limitations that can be addressed in future research. Firstly, owing to the pressure limitations of the



(a) Helical perforation fracturing-completion model **(b)** Simplified experimental model

Fig. 23. Schematic of helical perforation fracturing-completion model and simplified experimental model for horizontal section of shale gas reservoirs.

pump employed in the experiments, the geo-stress values adopted in the SC-CO_2 fracturing tests of this study were relatively low, which was different from the actual high stress conditions of deep shale reservoirs. The experimental results demonstrated that under low geo-stress conditions, CO_2 phase transition induced the formation of a multi-branched fracture network within the shale specimens. However, the extent to which CO_2 phase transition affects fracture propagation behavior under the constraints of high geo-stress remains to be further investigated. Secondly, although this study examined the effects of normal faulting and strike-slip faulting stress regimes on fracture propagation behavior, the small difference between the vertical principal stress and maximum horizontal principal stress resulted in experimental outcomes indicating that fracture propagation direction was still significantly dominated by bedding planes. Therefore, future fracturing tests can enlarge the difference between the vertical principal stress and the maximum horizontal principal stress to comprehensively clarify the effect of stress regimes (normal faulting or strike-slip faulting) on fracture propagation behavior.

6. Conclusions

In this study, a series of laboratory true triaxial fracturing experiments were conducted on the Longmaxi Formation shale. The 3D reconstruction of minute fractures induced by SC-CO_2 fracturing was achieved through the integration of the U-Net model with the CT technology, and the fracture characteristics were digitally quantified. Furthermore, the types of microcracks generated during fracturing experiments were identified with the help of AE technology. This study focused on the influence of the fluid type, horizontal stress differences and stress regimes on the fracturing-induced fracture characteristics and fracture propagation behavior of shale specimens. The main conclusions of this study are as follows.

(1) Compared with water fracturing, SC-CO_2 fracturing could significantly reduce the breakdown pressure of shale specimens and was capable of forming rougher fracture surfaces and more complex fracture networks. The results of 3D fracture reconstruction clearly demonstrated that the ability of SC-CO_2 to activate bedding planes and the phase transition effect of CO_2 were the two core mechanisms responsible for the generation of such rough and complex fractures during SC-CO_2 fracturing. However, if SC-CO_2 fracturing activated highly connected weak bedding planes in shale, the CO_2 fluid might leak directly along the opened bedding planes, thereby greatly reducing the enhanced effect of fracturing induced by CO_2 phase transition.

(2) As the horizontal stress difference increased, the fracture propagation behavior of shale in SC-CO_2 fracturing experiments gradually shifted from being dominated by bedding planes to being dominated by geo-stress. Under low stress difference coefficients, SC-CO_2 fracturing not only opened the shale bedding planes but also formed oblique main fractures in the shale matrix. The fracture initiation stage was dominated by shear cracks, whose main role was to activate bedding planes. The fracture propagation stage was dominated by tensile cracks, which promoted the fracture extension and network construction; under moderate stress difference coefficients, SC-CO_2 fracturing still generated oblique main fractures in the shale matrix, but its ability to preferentially activate bedding planes was weakened; under a high stress difference coefficient, SC-CO_2 fracturing produced main fractures approximately perpendicular to the minimum principal stress. Additionally, a large horizontal stress difference coefficient would reduce the roughness and complexity of fractures induced by SC-CO_2 fracturing.

(3) The stress regimes (normal faulting or strike-slip faulting) exerted minimal influence on the complexity of the fracture network because of the small magnitude difference between the maximum and intermediate principal stresses. The fracture propagation behavior of shale under the above two stress regimes remained significantly governed by the bedding plane. In addition, fracture propagation patterns when a fracture induced by SC-CO_2 fracturing approached a shale bedding plane were summarized, namely activating, deflecting, penetrating, and composite.

CRediT authorship contribution statement

Wang-Xing Hong: Writing – original draft, Validation, Software, Methodology, Investigation, Data curation, Conceptualization. **Sheng-Qi Yang:** Writing – review & editing, Project administration, Methodology, Investigation, Funding acquisition, Conceptualization. **Bo-Wen Sun:** Validation, Methodology, Investigation. **Xiao-Hua Xu:** Validation, Methodology. **Chao Zhu:** Methodology, Investigation. **Wen-Ling Tian:** Validation, Methodology. **P.G. Ranjith:** Writing – review & editing, Methodology.

Data availability

Data will be made available on request.

Declaration of competing interest

The authors declare that they have no known competing financial interests or personal relationships that could have appeared to influence the work reported in this paper.

Acknowledgments

This research was supported by the Jiangsu Province International Collaboration Program-Key National Industrial Technology Research and Development Cooperation Project (BZ2024023) and the National Natural Science Foundation of China (42477161).

References

Abdelaziz, A., Grasselli, G., 2024. Crack opening and slippage signatures during stimulation of bedded montney rock under laboratory true-triaxial hydraulic fracturing experiments. Rock Mech. Rock Eng. 57 (11), 9827–9845. https://doi.org/10.1007/s00603-024-04048-5.

Ai, T., Zhang, R., Zhou, H.W., et al., 2014. Box-counting methods to directly estimate the fractal dimension of a rock surface. Appl. Surf. Sci. 314, 610–621. https://doi.org/10.1016/j.apsusc.2014.06.152.

Al Shafloot, T., Kim, T.W., Kovscek, A.R., 2021. Investigating fracture propagation characteristics in shale using Sc-CO_2 and water with the aid of X-ray computed tomography. J. Nat. Gas Sci. Eng. 92, 103736. https://doi.org/10.1016/j.jngse.2020.103736.

Bennour, Z., Ishida, T., Nagaya, Y., et al., 2015. Crack extension in hydraulic fracturing of shale cores using viscous oil, water, and liquid carbon dioxide. Rock Mech. Rock Eng. 48 (4), 1463–1473. https://doi.org/10.1007/s00603-015-0774-2.

Cong, R.C., Yang, R.Y., Jing, M.Y., et al., 2024. Experimental investigation on hydraulic fracture propagation behaviors of coal-measure thin interbedded rocks. Rock Mech. Rock Eng. 57 (11), 9557–9573. https://doi.org/10.1007/s00603-024-04013-2.

Dan, X., Hu, R.L., Gao, W., et al., 2015. Effects of laminated structure on hydraulic fracture propagation in shale. Petrol. Explor. Dev. 42 (4), 573–579. https://doi.org/10.1016/S1876-3804(15)30052-5.

Estrada, J.M., Bhamidimarri, R., 2016. A review of the issues and treatment options for wastewater from shale gas extraction by hydraulic fracturing. Fuel 182, 292–303. https://doi.org/10.1016/j.fuel.2016.05.051.

Fleiss, J.L., Levin, B., Paik, M.C., 2003. Statistical Methods for Rates and Proportions. John Wiley & Sons, Inc., Hoboken. https://doi.org/10.1002/0471445428.

Gadelmawla, E.S., Koura, M.M., Maksoud, T.M.A., et al., 2002. Roughness parameters. J. Mater. Process. Technol. 123 (1), 133–145. https://doi.org/10.1016/S0924-0136(02)00060-2.
Gong, X., Jin, Z.J., Ma, X.H., et al., 2025. Effect of bedding structures on hydraulic fracture propagation behavior investigated using a coupled thermo-hydraulic-mechanical numerical model based on the phase-field cohesive zone method. Comput. Geotech. 186, 107427. https://doi.org/10.1016/j.compgeo.2025.107427.
Guo, P., Li, X., Li, S.D., et al., 2021. Quantitative analysis of anisotropy effect on hydrofracturing efficiency and process in shale using X-ray computed tomography and acoustic emission. Rock Mech. Rock Eng. 54 (11), 5715–5730. https://doi.org/10.1007/s00603-021-02589-7.
He, C.D., Sadeghpour, H., Shi, Y.X., et al., 2024. Mapping distribution of fractures and minerals in rock samples using Res-VGG-UNet and threshold segmentation methods. Comput. Geotech. 175, 106675. https://doi.org/10.1016/j.compgeo.2024.106675.
Hossain, M.M., Rahman, M.K., Rahman, S.S., 2000. Hydraulic fracture initiation and propagation: roles of wellbore trajectory, perforation and stress regimes. J. Pet. Sci. Eng. 27, 129–149. https://doi.org/10.1016/S0920-4105(00)00056-5.
Hou, B., Cui, Z., 2023. Vertical fracture propagation behavior upon supercritical carbon dioxide fracturing of multiple layers. Eng. Fract. Mech. 277, 108913. https://doi.org/10.1016/j.engfracmech.2022.108913.
Hou, B., Zhang, R.X., Zeng, Y.J., et al., 2018. Analysis of hydraulic fracture initiation and propagation in deep shale formation with high horizontal stress difference. J. Pet. Sci. Eng. 170, 231–243. https://doi.org/10.1016/j.petrol.2018.06.060.
Hu, Y., Liu, F., Hu, Y.Q., et al., 2019. Propagation characteristics of supercritical carbon dioxide induced fractures under true tri-axial stresses. Energies 12 (22), 4229. https://doi.org/10.3390/en12224229.
Iassonov, P., Gebrenegus, T., Tuller, M., 2009. Segmentation of X-ray computed tomography images of porous materials: a crucial step for characterization and quantitative analysis of pore structures. Water Resour. Res. 45 (9). https://doi.org/10.1029/2009WR008087.
Intergovernmental Panel on Climate Change (IPCC), 2022. Global Warming of 1.5°C: IPCC Special Report on Impacts of Global Warming of 1.5°C Above Pre-industrial Levels in Context of Strengthening Response to Climate Change, Sustainable Development, and Efforts to Eradicate Poverty. Cambridge University Press, Cambridge. https://doi.org/10.1017/9781009157940.
Ishida, T., Aoyagi, K., Niwa, T., et al., 2012. Acoustic emission monitoring of hydraulic fracturing laboratory experiment with supercritical and liquid CO_2. Geophys. Res. Lett. 39, L16309. https://doi.org/10.1029/2012GL052788.
Ishida, T., Chen, Y., Bennour, Z., et al., 2016. Features of CO_2 fracturing deduced from acoustic emission and microscopy in laboratory experiments. J. Geophys. Res. Solid Earth 121, 8080–8098. https://doi.org/10.1002/2016JB013365.
Jia, Y.Z., Lu, Y.Y., Elsworth, D., et al., 2018. Surface characteristics and permeability enhancement of shale fractures due to water and supercritical carbon dioxide fracturing. J. Pet. Sci. Eng. 165, 284–297. https://doi.org/10.1016/j.petrol.2018.02.018.
Jiang, Y.D., Qin, C., Kang, Z.P., et al., 2018. Experimental study of supercritical CO_2 fracturing on initiation pressure and fracture propagation in shale under different triaxial stress conditions. J. Nat. Gas Sci. Eng. 55, 382–394. https://doi.org/10.1016/j.jngse.2018.04.022.
Jiang, Y.L., Liang, W.G., Cai, T.T., et al., 2023. Fracture growth and acoustic emission response in natural coal-rock blocks with different stress, fracturing medium and injection rates. J. Pet. Sci. Eng. 220, 111228. https://doi.org/10.1016/j.petrol.2022.111228.
Jin, W.H., Jing, C., Wen, R., et al., 2024. Three-dimensional in-situ stress prediction based on pre-stack rock mechanics parameter inversion: a case study of shale gas in changning block. Comput. Tech. Geophys. Geochem. Explor. 46 (1), 11–25. https://doi.org/10.3969/j.issn.1001-1749.2024.01.02 (in Chinese).
Josifovic, A., Roberts, J.J., Corney, J., et al., 2016. Reducing the environmental impact of hydraulic fracturing through design optimisation of positive displacement pumps. Energy 115, 1216–1233. https://doi.org/10.1016/j.energy.2016.09.016.
Kingma, D.P., Ba, J., 2014. Adam: a method for stochastic optimization. arXiv preprint arXiv:1412.6980. https://doi.org/10.48550/arXiv.1412.6980.
Kumar, N., Verma, A., Ahmad, T., et al., 2024. Carbon capture and sequestration technology for environmental remediation: a CO_2 utilization approach through EOR. Geoenergy Sci. Eng. 234, 212619. https://doi.org/10.1016/j.geoen.2023.212619.
Lei, J., Fan, Y.F., 2024. Rock CT image fracture segmentation based on convolutional neural networks. Rock Mech. Rock Eng. 57 (8), 5883–5898. https://doi.org/10.1007/s00603-024-03824-7.
Li, B.X., Chu, X., Lin, F.S., et al., 2024. A highly efficient tunnel lining crack detection model based on mini-unet. Sci. Rep. 14 (1), 28234. https://doi.org/10.1038/s41598-024-79919-6.
Li, D.Q., Zhang, S.C., Zhang, S.A., 2014. Experimental and numerical simulation study on fracturing through interlayer to coal seam. J. Nat. Gas Sci. Eng. 21, 386–396. https://doi.org/10.1016/j.jngse.2014.08.022.
Li, S.B., Zhang, D.X., 2019. How effective is carbon dioxide as an alternative fracturing fluid? SPE J. 24 (2), 857–876. https://doi.org/10.2118/194198-PA.
Li, S.H., Zhang, S.C., Ma, X.F., et al., 2019. Hydraulic fractures induced by water-/carbon dioxide-based fluids in tight sandstones. Rock Mech. Rock Eng. 52 (9), 3323–3340. https://doi.org/10.1007/s00603-019-01777-w.
Liu, R., Zheng, J., Hao, F., et al., 2020. Variation in pore systems with tectonic stress in the overthrust Wufeng-Longmaxi shale of the southern Sichuan Basin, China. J. Nat. Gas Sci. Eng. 83, 103617. https://doi.org/10.1016/j.jngse.2020.103617.
Llanos, E.M., Jeffrey, R.G., Hillis, R., et al., 2017. Hydraulic fracture propagation through an orthogonal discontinuity: a laboratory, analytical and numerical study. Rock Mech. Rock Eng. 50, 2101–2118. https://doi.org/10.1007/s00603-017-1213-3.
Lu, J., Li, L.C., Lu, T.L., et al., 2025. Vertical propagation behavior of hydraulic fractures and multi-factor optimization of layered shale models using CT technology and the response surface method. Rock Mech. Rock Eng. 59, 401–436. https://doi.org/10.1007/s00603-025-04857-2.
Lyu, Q., Tan, J.Q., Li, L., et al., 2021. The role of supercritical carbon dioxide for recovery of shale gas and sequestration in gas shale reservoirs. Energy Environ. Sci. 14 (8), 4203–4227. https://doi.org/10.1039/D0EE03648J.
Middleton, R., Viswanathan, H., Currier, R., et al., 2014. CO_2 as a fracturing fluid: potential for commercial-scale shale gas production and CO_2 sequestration. Energy Proc. 63, 7780–7784. https://doi.org/10.1016/j.egypro.2014.11.812.
Middleton, R.S., Carey, J.W., Currier, R.P., et al., 2015. Shale gas and non-aqueous fracturing fluids: opportunities and challenges for supercritical CO_2. Appl. Energy 147, 500–509. https://doi.org/10.1016/j.apenergy.2015.03.023.
Mojid, M.R., Negash, B.M., Abdulelah, H., et al., 2021. A state–of–art review on waterless gas shale fracturing technologies. J. Pet. Sci. Eng. 196, 108048. https://doi.org/10.1016/j.petrol.2020.108048.
Nicot, J.P., Scanlon, B.R., 2012. Water use for shale-gas production in Texas, US. Environ. Sci. Technol. 46 (6), 3580–3586. https://doi.org/10.1021/es204602t.
Pei, P., Ling, K.G., He, J., et al., 2015. Shale gas reservoir treatment by a CO_2-based technology. J. Nat. Gas Sci. Eng. 26, 1595–1606. https://doi.org/10.1016/j.jngse.2015.03.026.
Pham, C., Zhuang, L., Yeom, S., et al., 2023. Automatic fracture characterization in CT images of rocks using an ensemble deep learning approach. Int. J. Rock Mech. Min. Sci. 170, 105531. https://doi.org/10.1016/j.ijrmms.2023.105531.
Qiu, G.Z., Chang, X., Li, J., et al., 2024. Study on the interaction between hydraulic fracture and natural fracture under high stress. Theor. Appl. Fract. Mech. 130, 104259. https://doi.org/10.1016/j.tafmec.2024.104259.
Ramandi, H.L., Mostaghimi, P., Armstrong, R.T., et al., 2016. Porosity and permeability characterization of coal: a micro-computed tomography study. Int. J. Coal Geol. 154, 57–68. https://doi.org/10.1016/j.coal.2015.10.001.
Rani, S., Padmanabhan, E., Prusty, B.K., 2019. Review of gas adsorption in shales for enhanced methane recovery and CO_2 storage. J. Pet. Sci. Eng. 175, 634–643. https://doi.org/10.1016/j.petrol.2018.12.081.
Ranjith, P.G., Zhang, C.P., Zhang, Z.Y., 2019. Experimental study of fracturing behaviour in ultralow permeability formations: a comparison between CO_2 and water fracturing. Eng. Fract. Mech. 217, 106541. https://doi.org/10.1016/j.engfracmech.2019.106541.
Reig, P., Luo, T.Y., Proctor, J.N., 2014. Global Shale Gas Development: Water Availability and Business Risks. World Resources Institute, Washington, D.C.
Ronneberger, O., Fischer, P., Brox, T., 2015. U-Net: Convolutional networks for biomedical image segmentation. In: International Conference on Medical Image Computing and Computer-Assisted Intervention. Springer, pp. 234–241. https://doi.org/10.1007/978-3-319-24574-4_28.
Rubin, E.S., Davison, J.E., Herzog, H.J., 2015. The cost of CO_2 capture and storage. Int. J. Greenh. Gas Control 40, 378–400. https://doi.org/10.1016/j.ijggc.2015.05.018.
Rumelhart, D.E., Hinton, G.E., Williams, R.J., 1986. Learning representations by back-propagating errors. Nature 323 (6088), 533–536. https://doi.org/10.1038/323533a0.
Satopaa, V., Albrecht, J., Irwin, D., et al., 2011. Finding a "kneedle" in a haystack: detecting knee points in system behavior. In: 2011 31st International Conference on Distributed Computing Systems Workshops. IEEE, pp. 166–171. https://doi.org/10.1109/ICDCSW.2011.20.
Scanlon, B.R., Reedy, R.C., Nicot, J.P., 2014. Comparison of water use for hydraulic fracturing for unconventional oil and gas versus conventional oil. Environ. Sci. Technol. 48 (20), 12386–12393. https://doi.org/10.1021/es502506v.
Shi, W.R., Wang, X.Z., Guo, M.Y., et al., 2020. Water use for shale gas development in China's fuling shale gas field. J. Clean. Prod. 256, 120680. https://doi.org/10.1016/j.jclepro.2020.120680.
Stueck, H., Houseknecht, D., Franke, D., et al., 2016. Shale-gas assessment: comparison of gas-in-place versus performance-based approaches. Nat. Resour. Res. 25 (3), 315–329. https://doi.org/10.1007/s11053-015-9283-y.
Sun, Y.X., Wang, X.L., Meng, Y.Z., et al., 2025. Fracture propagation mechanism and application of supercritical CO_2 fracturing in shale: a review. Pet. Sci. 22 (4), 1625–1652. https://doi.org/10.1016/j.petsci.2025.01.009.
Tan, P., Chen, Z.W., Huang, L.K., et al., 2024. Evaluation of the combined influence of geological layer property and in-situ stresses on fracture height growth for layered formations. Pet. Sci. 21 (5), 3222–3236. https://doi.org/10.1016/j.petsci.2024.07.014.
Tan, P., Jin, Y., Han, K., et al., 2017. Analysis of hydraulic fracture initiation and vertical propagation behavior in laminated shale formation. Fuel 206, 482–493. https://doi.org/10.1016/j.fuel.2017.05.033.
Tan, P., Jin, Y., Hou, B., et al., 2018. Laboratory investigation of shale rock to identify fracture propagation in vertical direction to bedding. J. Geophys. Eng. 15 (3), 696–706. https://doi.org/10.1088/1742-2140/aaa5d6.
Tang, K.N., Wang, Y.D., Mostaghimi, P., et al., 2022. Deep convolutional neural network for 3D mineral identification and liberation analysis. Miner. Eng. 183, 107592. https://doi.org/10.1016/j.mineng.2022.107592.
Tian, Y.J., Wang, D.G., Xia, J., et al., 2025. Digital rock modeling of deformed multi-scale media in deep hydrocarbon reservoirs based on in-situ stress-loading CT imaging and U-Net deep learning. Mar. Petrol. Geol. 171, 107177. https://doi.org/10.1016/j.marpetgeo.2024.107177.

Van Eijnatten, M., van Dijk, R., Dobbe, J., et al., 2018. CT image segmentation methods for bone used in medical additive manufacturing. Med. Eng. Phys. 51, 6–16. https://doi.org/10.1016/j.medengphy.2017.10.008.

Wang, J.X., Liang, P., Zhang, Y.B., et al., 2024. Research on classification of rock tensile-shear fracture based on acoustic emission RA-AF values and kneedle algorithm. Chin. J. Rock Mech. Eng. 43 (S1), 3267–3279. https://doi.org/10.13722/j.cnki.jrme.2023.0696 (in Chinese).

Wang, L., Yao, B.W., Xie, H.J., et al., 2017. CO_2 injection-induced fracturing in naturally fractured shale rocks. Energy 139, 1094–1110. https://doi.org/10.1016/j.energy.2017.08.031.

Wu, S., Ge, H.K., Li, T.T., et al., 2022. Characteristics of fractures stimulated by supercritical carbon dioxide fracturing in shale based on acoustic emission monitoring. Int. J. Rock Mech. Min. Sci. 152, 105065. https://doi.org/10.1016/j.ijrmms.2022.105065.

Xie, Z.X., Wu, X.G., Long, T.D., et al., 2023. Visualization of hydraulic fracture interacting with pre-existing fracture. Pet. Sci. 20 (6), 3723–3735. https://doi.org/10.1016/j.petsci.2023.07.014.

Yang, B., Huang, H., Ren, Q.Q., et al., 2025a. Quantitative insight into fracture distribution during supercritical CO_2 fracturing on tight sandstone formation. Pet. Sci. 22 (4), 1670–1685. https://doi.org/10.1016/j.petsci.2025.02.006.

Yang, B., Wang, H.Z., Wang, B., et al., 2021. Digital quantification of fracture in full-scale rock using micro-CT images: a fracturing experiment with N_2 and CO_2. J. Petrol. Sci. Eng. 196, 107682. https://doi.org/10.1016/j.petrol.2020.107682.

Yang, S.Q., Cao, M.H., Yong, R., et al., 2025b. Experimental investigation on mechanical behaviors and shear fracture mechanisms of rough jointed sandstone under conventional triaxial compression. Int. J. Rock Mech. Min. Sci. 194, 106205. https://doi.org/10.1016/j.ijrmms.2025.106205.

Yang, S.Q., Hong, W.X., Wang, J.G., et al., 2024. Experimental investigation on the influence of NaCl concentration on triaxial mechanical behaviors of a low-clay shale. Int. J. Rock Mech. Min. Sci. 176, 105716. https://doi.org/10.1016/j.ijrmms.2024.105716.

Yang, S.Q., Yin, P.F., Ranjith, P.G., 2020. Experimental study on mechanical behavior and brittleness characteristics of Longmaxi Formation shale in Changning, Sichuan Basin, China. Rock Mech. Rock Eng. 53, 2461–2483. https://doi.org/10.1007/s00603-020-02057-8.

Yeung, M., Rundo, L., Nan, Y., et al., 2023. Calibrating the dice loss to handle neural network overconfidence for biomedical image segmentation. J. Digit. Imag. 36 (2), 739–752. https://doi.org/10.1007/s10278-022-00735-3.

Zang, Y.X., Wang, H.Z., Wang, B., et al., 2024. In-situ laboratory study on influencing factors of pre-SC-CO_2 hybrid fracturing effect in shale oil reservoirs. Pet. Sci. 21 (5), 3547–3557. https://doi.org/10.1016/j.petsci.2024.05.020.

Zhang, J., Yu, Q.G., Li, Y.W., et al., 2023. Hydraulic fracture vertical propagation mechanism in interlayered brittle shale formations: an experimental investigation. Rock Mech. Rock Eng. 56 (1), 199–220. https://doi.org/10.1007/s00603-022-03094-1.

Zhang, K., Liu, X.F., Wang, D.B., et al., 2024. A review of reservoir damage during hydraulic fracturing of deep and ultra-deep reservoirs. Pet. Sci. 21 (1), 384–409. https://doi.org/10.1016/j.petsci.2023.11.017.

Zhang, X.W., Lu, Y.Y., Tang, J.R., et al., 2017. Experimental study on fracture initiation and propagation in shale using supercritical carbon dioxide fracturing. Fuel 190, 370–378. https://doi.org/10.1016/j.fuel.2016.10.120.

Zhang, Y.L., Liu, Z.B., Han, B., et al., 2022. Numerical study of hydraulic fracture propagation in inherently laminated rocks accounting for bedding plane properties. J. Pet. Sci. Eng. 210, 109798. https://doi.org/10.1016/j.petrol.2021.109798.

Zhang, Y.X., He, J.M., Li, X., et al., 2019. Experimental study on the supercritical CO_2 fracturing of shale considering anisotropic effects. J. Pet. Sci. Eng. 173, 932–940. https://doi.org/10.1016/j.petrol.2018.10.092.

Zhao, X.R., Chen, Z.M., Wang, B., et al., 2023. A Multi-medium and Multi-mechanism model for CO_2 injection and storage in fractured shale gas reservoirs. Fuel 345, 128167. https://doi.org/10.1016/j.fuel.2023.128167.

Zhao, Z.H., Li, X., He, J.M., et al., 2018. A laboratory investigation of fracture propagation induced by supercritical carbon dioxide fracturing in continental shale with interbeds. J. Pet. Sci. Eng. 166, 739–746. https://doi.org/10.1016/j.petrol.2018.03.066.

Zheng, Y., Zhou, M.M., Kuru, E., et al., 2024. Proppant transport in rough fracture networks using supercritical CO_2. Pet. Sci. 21 (3), 1852–1864. https://doi.org/10.1016/j.petsci.2024.03.023.

Zhong, Y.L., Yu, H., Wang, Q., et al., 2024. Hydraulic fracturing in layered heterogeneous shale: the interaction between adjacent weak interfaces. Eng. Fract. Mech. 303, 110115. https://doi.org/10.1016/j.engfracmech.2024.110115.

Zhou, D.W., Zhang, G.Q., Wang, Y.Y., et al., 2018a. Experimental investigation on fracture propagation modes in supercritical carbon dioxide fracturing using acoustic emission monitoring. Int. J. Rock Mech. Min. Sci. 110, 111–119. https://doi.org/10.1016/j.ijrmms.2018.07.010.

Zhou, D.W., Zhang, G.Q., Zhao, P.Y., et al., 2018b. Effects of post-instability induced by supercritical CO_2 phase change on fracture dynamic propagation. J. Pet. Sci. Eng. 162, 358–366. https://doi.org/10.1016/j.petrol.2017.12.066.

Zhou, J.P., Hu, N., Xian, X.F., et al., 2019. Supercritical CO_2 fracking for enhanced shale gas recovery and CO_2 sequestration: results, status and future challenges. Adv. Geo-Energy Res. 3 (2), 207–224. https://doi.org/10.26804/ager.2019.02.10.

Zhou, J.P., Liu, G.J., Jiang, Y.D., et al., 2016. Supercritical carbon dioxide fracturing in shale and the coupled effects on the permeability of fractured shale: an experimental study. J. Nat. Gas Sci. Eng. 36, 369–377. https://doi.org/10.1016/j.jngse.2016.10.005.

Zhou, Q., Xie, H.P., Zhu, Z.M., et al., 2023. Fracture toughness anisotropy in shale under deep *in situ* stress conditions. Rock Mech. Rock Eng. 56 (10), 7535–7555. https://doi.org/10.1007/s00603-023-03454-5.

Zou, Y.S., Zhang, S.C., Zhou, T., et al., 2016. Experimental investigation into hydraulic fracture network propagation in gas shales using CT scanning technology. Rock Mech. Rock Eng. 49 (1), 33–45. https://doi.org/10.1007/s00603-015-0720-3.

Zou, Y.S., Li, N., Ma, X.F., et al., 2018. Experimental study on the growth behavior of supercritical CO_2-induced fractures in a layered tight sandstone formation. J. Nat. Gas Sci. Eng. 49, 145–156. https://doi.org/10.1016/j.jngse.2017.11.005.